

© Copyright by Benedict Isichei 2018
All Rights Reserved

ROBOTIC MANIPULATORS:
CRYOGENIC MAGNETIC MANIPULATION SYSTEM, TWO-BODY
MAGNETIC MANIPULATION, AND LOW-COST ROBOTIC
MANIPULATORS

A Thesis

Presented to

the Faculty of the Department of Electrical and Computer Engineering

University of Houston

in Partial Fulfillment

of the Requirements for the Degree

Master of Science

in Electrical Engineering

by

Benedict Isichei

August 2018

ROBOTIC MANIPULATORS:
CRYOGENIC MAGNETIC MANIPULATION SYSTEM, TWO-BODY
MAGNETIC MANIPULATION, AND LOW-COST ROBOTIC
MANIPULATORS

Benedict Isichei

Approved:

Chair of the Committee
Aaron T. Becker, Assistant Professor
Department of Electrical and Computer Engineering

Committee Members:

David Mayerich, Assistant Professor
Department of Electrical and Computer Engineering

Rose Faghieh, Assistant Professor
Department of Electrical and Computer Engineering

Julien Leclerc, Postdoctoral researcher
Department of Electrical and Computer Engineering

Suresh K. Khator, Associate Dean,
Cullen College of Engineering

Badrinath Roysam, Professor and Chair,
Electrical and Computer Engineering

Acknowledgements

I would like to deeply thank the following people who played outstanding roles in the completion of this thesis. My immense gratitude goes to my indefatigable thesis committee chair, professor and mentor, Dr. Aaron T. Becker for his steadfast guidance, patience, encouragement and kindness while I was working on this thesis. I profoundly appreciate Dr. Julien Leclerc and Dr. Shiva Shahrokhi for their advice, directions, patience and coaching roles while I was working on their respective projects. I am extremely grateful to the various members of the swarm robotics lab for being there for me when I had issues and having no problems stepping in with explanations. Lastly, this note of acknowledgement would not be complete without recognizing my parents for their utter love, tireless encouragement and unswerving support.

ROBOTIC MANIPULATORS:
CRYOGENIC MAGNETIC MANIPULATION SYSTEM, TWO-BODY
MAGNETIC MANIPULATION, AND LOW-COST ROBOTIC
MANIPULATORS

An Abstract

of a

Thesis

Presented to

the Faculty of the Department of Electrical and Computer Engineering

University of Houston

in Partial Fulfillment

of the Requirements for the Degree

Master of Science

in Electrical Engineering

by

Benedict Isichei

August 2018

Abstract

This project presents three different robotic manipulators, and then compares their control systems. The first system is a cryogenically-cooled manipulation system. In this system, the robotic system implements 3-dimensional control on the robots position and orientation. To obtain accurate control without a solid iron core, this system has all of its coils cooled with liquid nitrogen to drive more current into the coils without damaging them. The second system is created to test an algorithm for navigation in a cavity using global inputs, while taking advantage of the cavitys geometry and frictional wall contacts. The last system is a robotic manipulator created out of a toy robotic arm kit. The aim here was to increase the robots accuracy and augment its functionality, while making it user friendly to students new to robotics.

Table of Contents

Acknowledgements	v
Abstract	vii
Table of Contents	viii
List of Figures	xi
List of Tables	xiv
1 Introduction	1
2 Cryogenic Manipulation System	3
2.1 INTRODUCTION	3
2.2 System Presentation	6
2.3 Cooling with Liquid Nitrogen	9
2.3.1 Motivations	9
2.3.2 Scaling Law	11
2.4 Inverse Magnetism	15
2.4.1 Forward problem	15
2.4.2 Inverse problem	17
2.5 Trajectory control	18
2.6 Singularities analysis for a 3-DOF robot	19

2.7	Experimental Results	22
2.8	Conclusion and Future Works	24
3	Two-Body Magnetic Manipulation with Global Inputs	26
3.1	Introduction	27
3.2	Related Work	28
3.3	Theory	29
3.3.1	Boundary Interaction Model	30
3.4	Experimental Results	30
3.4.1	Magnetic Manipulation Setup	31
3.4.2	Intestine Phantom Model	32
3.4.3	Bovine Stomach Cross-section	32
3.5	Conclusion and Future Work	33
4	Low-Cost Robot Manipulator Arms	34
4.1	Lab 1: Assembly and Familiarization	35
4.2	Lab 2: Open-Loop Control	36
4.3	Lab 3: Closed-loop Control with Potentiometer Sensors	37
4.4	Lab 4: Closed-loop Control with Image Processing	39
4.5	GUI	39
4.5.1	Configuration	40
4.5.2	Automation	41
4.6	Pre-semester Prep	41
4.7	Results	43

5 Conclusion	44
References	45

List of Figures

1.1	Top view of the magnetic manipulator, showing two of the side coils and one of the camera sensors	2
1.2	The phantom intestine model, used to simulate the small intestine of a cow along with its villi	2
2.1	Picture of the magnetic manipulator while functioning. Inset shows view from the camera used to obtain position feedback of the robot.	4
2.2	CAD model of the magnetic manipulator: (a) exploded view of three cryostats, (b) cross-section view.	8
2.3	Block diagram of (a) the physical hardware and (b) the controller used for position control.	9
2.4	3D representation of a dual-coil collinear EM assembly.	11
2.5	Maximum sustainable magnetic flux density by different EM designs. Magnet specifications are given in Table 2.1.	12
2.6	Plot of the winding volume (a) and power consumption (b) of air-cooled (300K) and LN2-cooled (77K) EMs.	15
2.7	Map of the conditioning of the actuation matrix \mathbf{A}_0 for (a) $\theta = 0$ and (f) $\theta = \pi/4$. Map of the norm of the total current needed to produce a force of 100 mN along the d axis (b, d, g and i) and along the q axis (c, e, h and j).	20
2.8	Plot of the trajectory of the robot obtained experimentally. For this dataset, the robot completed the path ten times. The robot and the workspace are shown at right.	22

2.9	Voltage, current, and power used during robot navigation. The curves show 60 seconds of data, which correspond to the robot completing the trajectory in Fig. 2.8 three times.	23
3.1	Workspace and magnetic setup for an experiment to position particles that receive the same control inputs, but cannot move while a control input pushes them into a boundary.	28
3.2	Frames showing particle positions before and after control inputs. Top row: small intestine phantom. Bottom row: cow stomach tissue.	31
4.1	The unmodified robotic arm	34
4.2	The parts of the robot arm before assembly	35
4.3	The assembled robotic arm	36
4.4	The custom PCB with initial configuration as a manual remote	36
4.5	Intermediate step in assembling the arm for open-loop control	37
4.6	Fully connected microcontroller, motor driver and PCB boards for open-loop control	37
4.7	The fabricated parts, and augmented joints	38
4.8	The augmented robotic arm	38
4.9	The graphical user interface, and the virtual remote control. To allow ease of access, the virtual remote is accessible from all tabs in the GUI, and can be used after the Arduino input/output pins have been set	39
4.10	The setup tab of the user interface. The program takes the user through the steps required to configure the input/output pins, and calibrate the robot's potentiometers	40

4.11	Limits used for calibrating the robot's sensors. By moving the robot to the known extremes of its joints, any value within the limits can be achieved with a simple mapping calculation	41
4.12	The automation tab of the GUI. The buttons on this tab help the user program different movement paths.	42

List of Tables

2.1	Description of the electromagnet designs compared in Fig. 2.5.	11
2.2	Comparison between EM properties at room temperature (300K) and at LN2 temperature (77K).	12

Chapter 1

Introduction

In the field of robotics, manipulation is an important aspect to all robotic systems. Regardless of its form factor, a robot's means of manipulation is an important factor that affects how it is controlled, and what applications it can be applied to. In this thesis, the manipulation systems of three different robots are presented and analyzed. The first robot presented, a magnetic manipulator cooled with liquid nitrogen, deals with a millimeter scale robot whose position and orientation are controlled by three pairs of electromagnetic coils placed orthogonal to each other. In this system, the manipulators are the 6 coils and their magnetic fields. In order to increase the strength of the fields in this system without using iron cores, each coil was cooled to cryogenic temperatures. By cooling the coils and reducing their resistances, more current can be driven into the coils and increase their fields proportionally. Fig. 1.1 shows a top view of the system with the top coil taken out. The second system presented in this thesis is a two dimensional manipulator system similar to the the first, but with a smaller workspace, and using solid iron cores to concentrate the magnetic field. This system was used to implement an algorithm to move a pair of 'robots' to predefined goal locations by taking advantage of the cavity's geometry, surface friction and global inputs to both robots. Fig. 1.2 shows one of the cavities, the phantom intestine model, used to test the algorithm. For the third and final system, the manipulator considered is a five degree of freedom robotic arm. The arm originally comes without any sensors on its joints, but through the addition of several fabricated parts and sensors, the arm's manipulability and functionality are increased significantly.

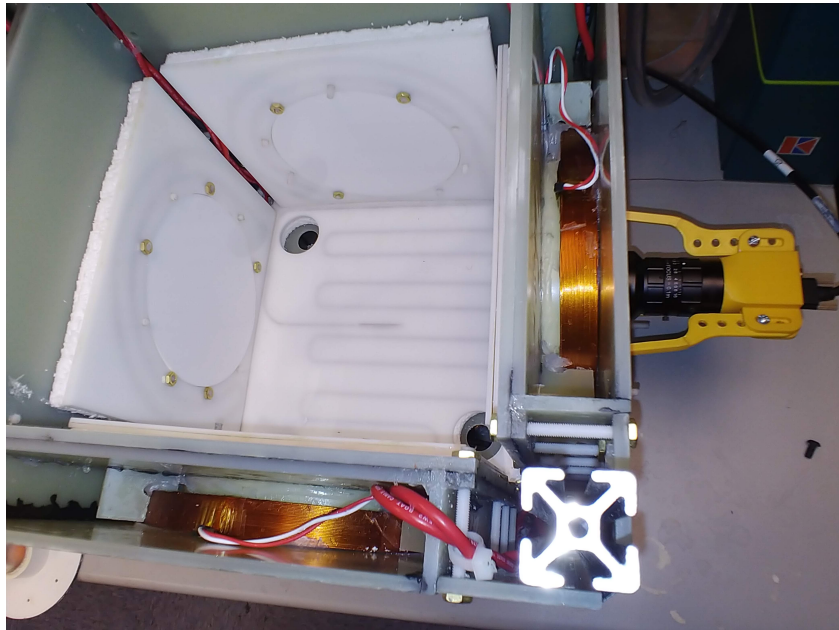


Figure 1.1: Top view of the magnetic manipulator, showing two of the side coils and one of the camera sensors



Figure 1.2: The phantom intestine model, used to simulate the small intestine of a cow along with its villi

Chapter 2

Cryogenic Manipulation System

This chapter is based on a Journal paper with Julien Leclerc, Benedict Isichei, and Aaron T. Becker. The author's contribution was in the design of the heating elements interfacing the Manipulator and the robotic workspace, creating a camera mount for the system's sensory feedback, and working on the object tracking. Nathan Hui aided with editing the final version of the paper.

2.1 INTRODUCTION

Magnetic actuation enables non-contact manipulation from a distance. This paper describes a magnetic manipulator, shown in Fig. 2.1, that uses coils cooled by liquid nitrogen to reduce the size and power required to generate dynamic magnetic fields. Magnetic technologies have promise for several areas, including as actuation for minimally invasive surgery [1, 2]. Minimally invasive surgeries reduce patient recovery time, pain, and risks of infection [3]. These procedures are most often performed using a catheter, a tubular device that can access remote areas of the body through small incisions. If all catheter actuation is applied at the proximal end, it is increasingly difficult to accurately control force and orientation of the distal tip as the length increases.

Magnetic actuation can be used to improve the effectiveness of minimally invasive surgeries. The company Stereotaxis [1] manufactures a magnetic system able to control the tip of a magnetic catheter and therefore increase the precision of the medical procedure. The device uses two permanent magnets rotating around the workspace.

Unfortunately, calcified fat deposits can build up inside arteries during the life of

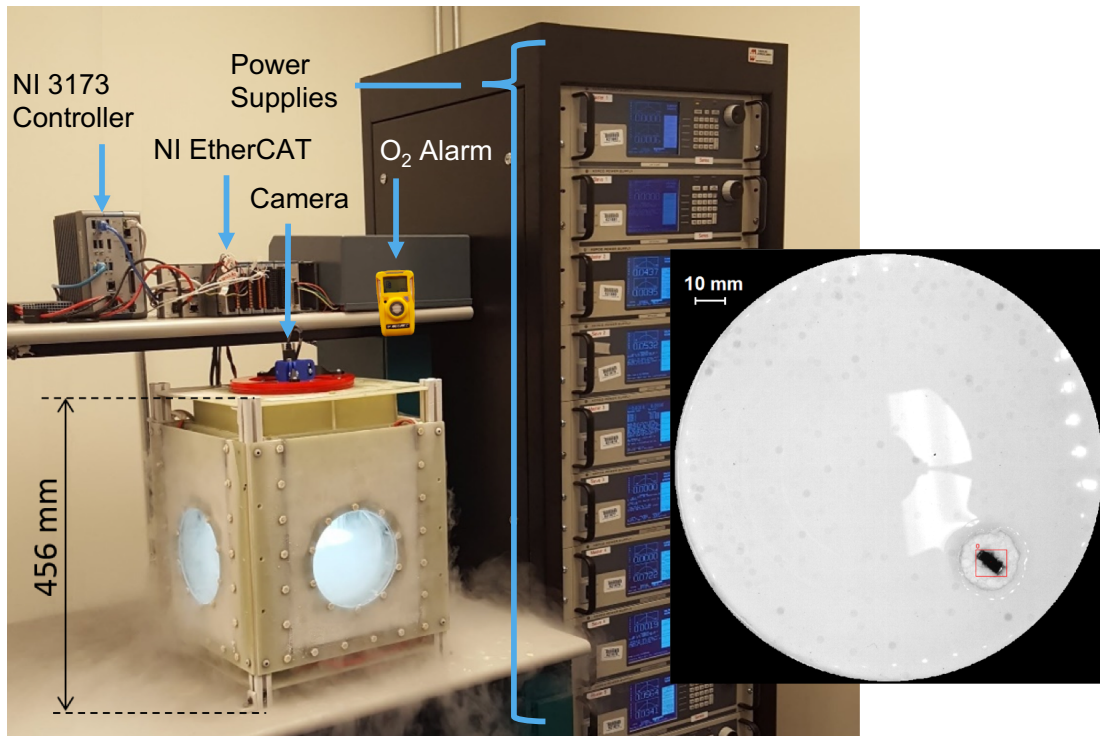


Figure 2.1: Picture of the magnetic manipulator while functioning. Inset shows view from the camera used to obtain position feedback of the robot.

a person, a condition called atherosclerosis [4]. These deposits, called *plaques*, may be detached by the friction between the catheter and the walls of the blood vessel and cause a stroke [5, 6].

Tetherless magnetic robots could further decrease the invasiveness of procedures [2]. The idea is to use external magnets to manipulate a small magnetic tool or capsule placed inside a patient. The absence of tethers and the ability to navigate without touching the blood vessel walls [7] reduces the risk of plaque detachment. A fast and accurate tracking method can enable precise control of the robot position during navigation. However, permanent magnets are limited by their maximum rotational speed and acceleration and are therefore often unsuitable for fast dynamic control. In contrast, electromagnets (EM) can generate magnetic fields with fast dynamics without moving parts. Their magnetic field change rate is limited by either the power of the generator or the maximum voltage

the magnet can sustain.

MRI scanners have EM and can be used as magnetic manipulators [8, 9, 10]. When a ferromagnetic piece (the robot) is placed inside this device, it becomes magnetized by the main magnetic field. Because the main field is approximately uniform (less than 1 ppm of inhomogeneity [11]), it does not produce significant forces on the robot. Instead, the MRI gradient coils can be used to produce a controlled force.

The major advantage of using of MRI scanners for magnetic manipulation is that they are already widely available in hospitals and the robot's position can be tracked in real-time using the MR signal [12, 10]. However, the large static magnetic field in an MRI permanently orients the magnetic field in the same direction, making torque control of robots impossible. The gradient coils can be used to generate forces on the robot.

Power consumption and heat dissipation are the primary limitations on EMs. The current circulating inside a conductor produces Joule losses. Electromagnetic field strength is limited by its maximum power dissipation density. More compact magnet designs can be achieved by reducing the amount of losses produced per unit of flux density. If power consumption is not a concern, the maximum power dissipation density can also be increased.

Adding a ferromagnetic core to an EM is an effective way to increase the magnetic field and the forces produced without increasing the losses. Cores enable increasing the inductance value which in turn increases the total flux produced per ampere. However, the use of a ferromagnetic core requires a closed bore geometry for the magnet. This is often an issue for medical applications. MRIs are designed with open bores on two opposite sides to accommodate the patient. Additional openings could allow medical staff to access the patient during the procedure and decrease feelings of claustrophobia.

Using liquid nitrogen (LN2) is another way to decrease the amount of losses produced per unit of flux density. This method decreases the value of the electrical resistivity

of copper and therefore allows more current to circulate inside the magnet for a given amount of losses. Cooling the EM to cryogenic temperatures offers another advantage: because the temperature of the coolant is low, the maximum safe temperature increase of the coil is larger. LN2 cooling therefore increases the maximum power dissipation density. LN2 is cheap (approximately 0.13 USD/Liter) and available in industrial quantities. It is non-toxic as gaseous nitrogen composes 78% of the volume of our atmosphere. However, if large quantities of liquid nitrogen are evaporated, the level of oxygen in the room might decrease. An adapted ventilation system and a low oxygen alarm must be used to prevent anoxia.

This paper presents the design and test of a magnetic manipulator cooled with LN2. A demonstration system is described in Section 2.2. The motivations and technical difficulties associated with this type of cooling are discussed in Section 2.3. A method to perform inverse magnetic calculations is then explained in Section 2.4. A robot trajectory controller is described in Section 2.5. Next the system singularities are analyzed for 3-DOF control of a permanent magnet in Section 2.6. Experimental results are presented and analyzed in Section 2.7. The paper concludes with lessons learned in this study.

2.2 System Presentation

The magnetic manipulator in Fig. 2.1 is designed to fit a human heart phantom. Detailed build instructions, a bill of materials, and CAD models are available¹. The working volume is a sphere with radius 0.075 m. The system is composed of six copper coils arranged in a cubical shape (see Fig. 2.2). Each coil is placed and held in an independent cryostat. The cryostats contain the LN2 and were built using G10. G10 is a fiberglass-epoxy composite able to withstand cryogenic temperatures. Ordinary plastics become brittle at cryogenics temperatures, but G10 remains resilient. G10 is

¹github.com/RoboticSwarmControl/magnetic-manipulator-l2n-source

also electrically nonconductive, an important feature to avoid induced currents. Induced currents generate a magnetic field that opposes variations in the applied field, making the system less responsive. Induced currents also generate heat.

Uninsulated G10 walls become cold and water present in air condenses and freezes on them. This ice could interfere with objects in the workspace. To prevent icing, the cryostat walls facing the workspace are insulated by a 10 mm thick layer of Styrofoam insulation. Six acrylic plates (one for each internal face) containing a resistive heater and a thermocouple temperature sensor cover the inner face of the insulation. The temperature of the internal walls surrounding the workspace are regulated using a real-time controller. The evaporation rate of LN2 is the product $\mathcal{L} \cdot P_o$, where \mathcal{L} is the latent heat of vaporization, equal to 200 kJ/kg for LN2 and P_o is the power dissipated. The maximum power consumption of each coil of the system is 2 kW. At maximum power, 0.74 liters of LN2 evaporate per minute.

12 Kepco BOP 20-50 generators power the system. Each power supply can generate 20 A under 50 V. Each coil is powered by two of these supplies connected in series. Each coil can, therefore, receive a maximum of 20 A under 100 V. Each set of power supplies is controlled via an analog input. While the current inside an EM is directly proportional to the magnetic flux density produced, the voltage applied on an EM is proportional to the time derivative of the flux density. It is therefore easier to control the produced magnetic field by controlling the current rather than the voltage on the EM. The BOP power supplies can do this when controlled in current mode. In this mode, the power supplies output a current proportional to an analog input.

An industrial controller IC-3173 from National Instrument is used for real-time computation, as shown in Fig. 2.3(a). A set of two Basler acA2040 cameras are attached at orthogonal faces of the magnetic manipulator. These cameras are used to obtain robot position and orientation in real-time (100 Hz). Two high precision NI 9263 analog

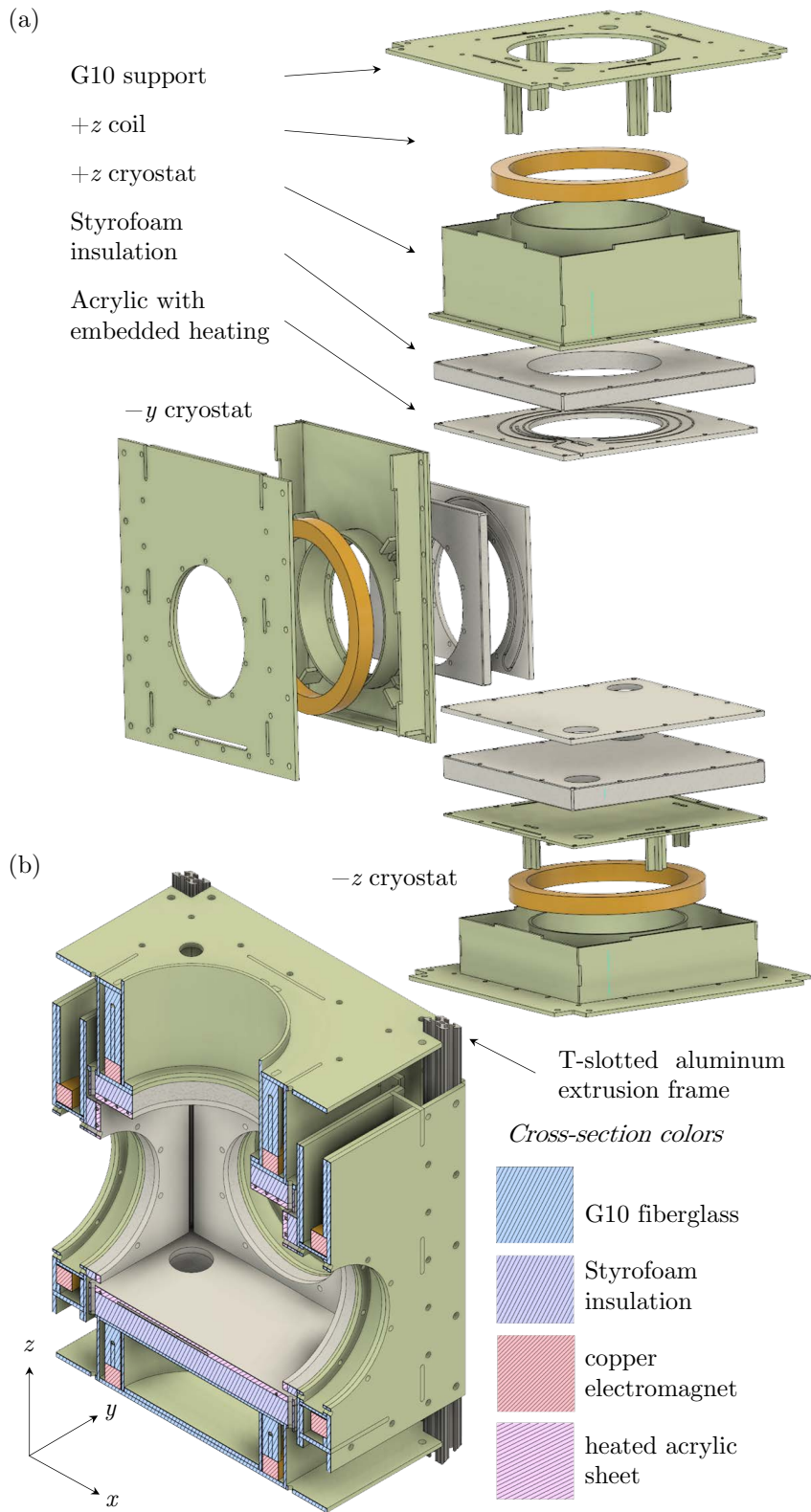


Figure 2.2: CAD model of the magnetic manipulator: (a) exploded view of three cryostats, (b) cross-section view.

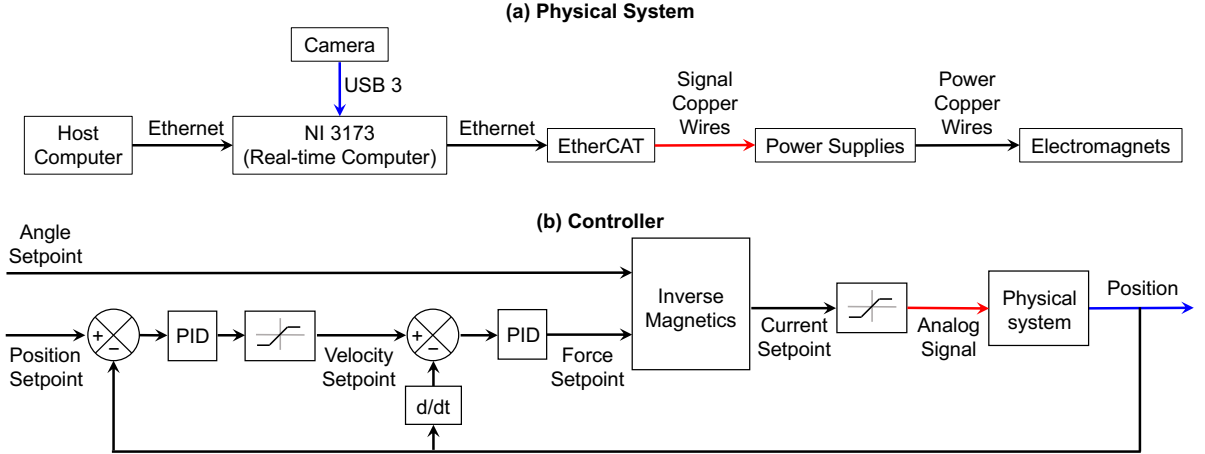


Figure 2.3: Block diagram of (a) the physical hardware and (b) the controller used for position control.

modules are used to generate the analog signal controlling the power supplies.

The laboratory is equipped with a low oxygen alarm (Honeywell BW Clip, approximately 140 USD).

2.3 Cooling with Liquid Nitrogen

2.3.1 Motivations

The voltage U_l at the terminals of a resistive coil can be calculated using the following equation:

$$U_l = L \cdot \frac{dI(t)}{dt} + R(t) \cdot I(t), \quad (2.1)$$

where I is the current in the coil, L is the coil inductance, and R is the coil resistance.

Two components are present in this equation:

- The term $L \cdot dI(t)/dt$ is related to the magnetic energy change rate. This term does not cause losses if a four quadrant power supply is used. This type of power supply has the ability to transfer stored magnetic energy back to the electrical network. It is desirable to maximize $L \cdot dI(t)/dt$ because a high magnetic energy change rate

generates a large force change rate, a desirable feature for robot control.

- The term $R(t) \cdot I(t)$ is associated with Joule losses. It is an undesirable term for two reasons. First, it causes the coil to heat and decreases the energy efficiency of the system. Secondly, power supplies are limited by their maximum voltage. The voltage across the coil is shared between the two terms of equation 2.1. If the term $R(t) \cdot I(t)$ is increased, less voltage is available for the term $L \cdot dI(t)/dt$. LN2 cooling allows reducing the value of $R(t)$ by 87%;

The magnetic flux Φ produced by a solenoid is proportional to its inductance as shown in

$$\Phi(t) = L \cdot I(t). \tag{2.2}$$

In [13], the authors use a ferromagnetic core to increase the value of L and therefore increase the amount of force generated. LN2 cooling is different and increases the generated field by increasing the value of $I(t)$. It is technically difficult to scale up magnetic manipulators [13]. Air-cooled human-size manipulators would use comparatively large electromagnets to produce the magnetic field. This technical challenge could potentially be solved using LN2 cooling. This type of cooling enables a significant decrease in the system price, size, mass and/or improve its energy efficiency.

This tendency is illustrated in Fig. 2.5 and Table 2.1, which compares the flux density magnitude produced by different EM designs along their revolution axis. The comparison was computed using the magnetic modeling software Finite Elements Method Magnetics (FEMM [14]). EM1 and EM3 correspond to the EM present in our experimental setup when respectively cooled with LN2 (EM1) and forced air (EM3). The gain of flux density and magnetic gradient when cooling with LN2 is +435% and is relatively equal to the gain in current (see Table 2.2). EM2 and EM4 correspond to the same EM as 1 and 3 except that ferromagnetic cores were added to each. The gain in flux density is small, approximately 10%. EM6 is a forced-air-cooled EM with a ferromagnetic core

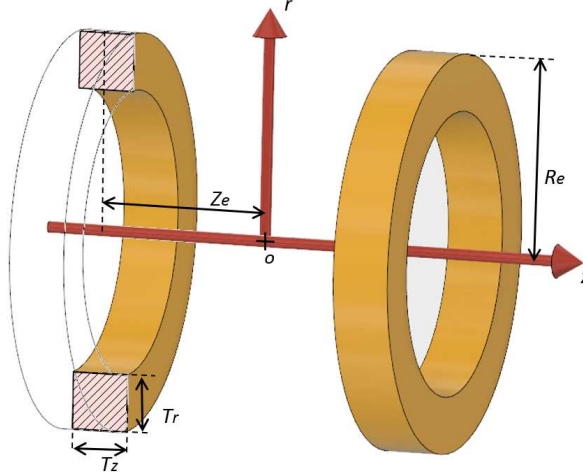
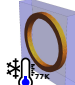
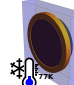






Figure 2.4: 3D representation of a dual-coil collinear EM assembly.

designed to generate the same magnetic field as EM1. EM6 must be $2.5\times$ longer than EM1. EM5 is the same as EM6 except that the ferromagnetic core was removed. The relative gain in flux density obtained by adding a ferromagnetic core is larger for EM5 and EM6, suggesting that the gain is related to the aspect ratio of length/diameter of the coil.

Table 2.1: Description of the electromagnet designs compared in Fig. 2.5.

Electromagnet ID	1	2	3	4	5	6
External radius R_e	110 mm	110 mm	110 mm	110 mm	110 mm	110 mm
Coil width T_r	20 mm	20 mm	20 mm	20 mm	20 mm	20 mm
Coil length T_z	20 mm	20 mm	20 mm	20 mm	50 mm	50 mm
Number of turns	795	795	795	795	1987	1987
Copper wire	AWG 22	AWG 22	AWG 22	AWG 22	AWG 22	AWG 22
Core	Air	Hyperco-50	Air	Hyperco-50	Air	Hyperco-50
Cooling method	LN2	LN2	Forced air	Forced air	Forced air	Forced air
Max. cont. current	7.5 A	7.5 A	1.4 A	1.4 A	1.4 A	1.4 A
Schematic						

2.3.2 Scaling Law

This section uses analytical equations to derive the gradient produced by two concentric electromagnets on their revolution axis (see Fig. 2.4). The electromagnets have an external radius R_e . They have a rectangular $T_z \times T_r$ cross-section. The filling factor

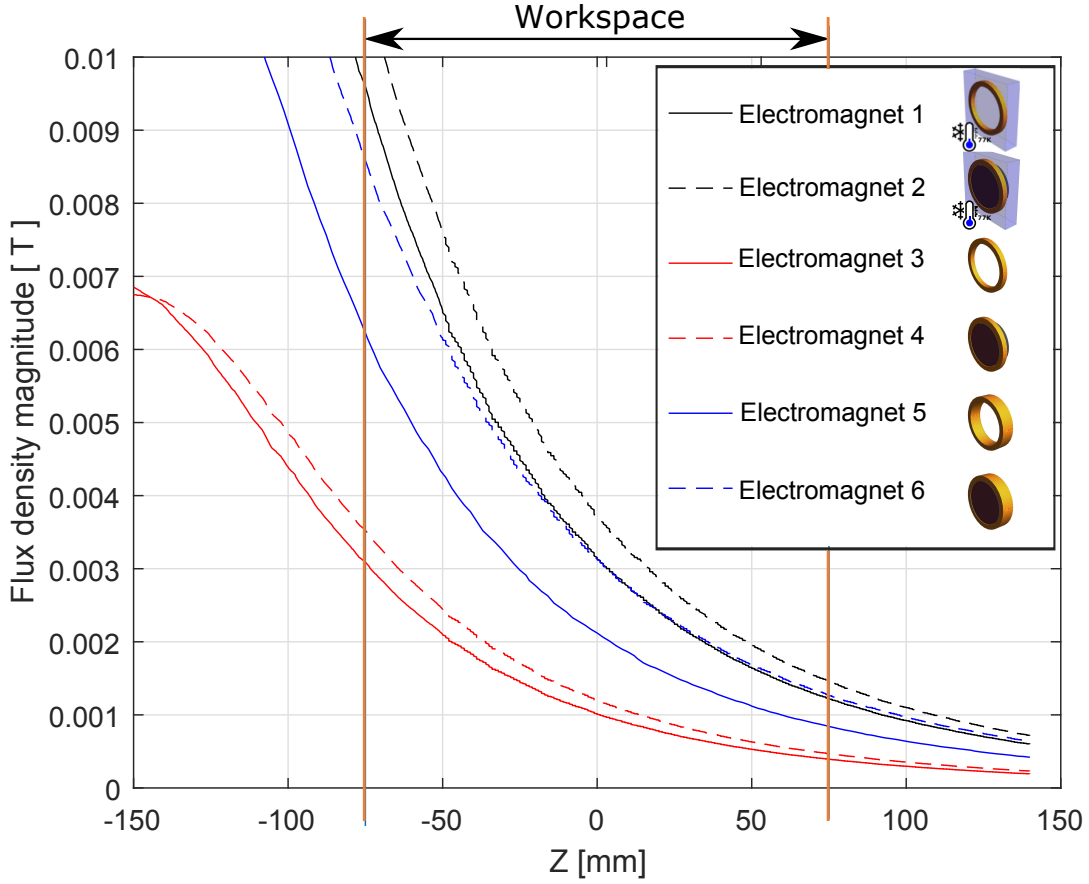


Figure 2.5: Maximum sustainable magnetic flux density by different EM designs. Magnet specifications are given in Table 2.1.

Table 2.2: Comparison between EM properties at room temperature (300K) and at LN2 temperature (77K).

	300K	77K	Difference
Copper electrical resistivity	1.68E-8 $\Omega \cdot \text{m}$	2.15E-9 $\Omega \cdot \text{m}$	-87%
Coil electrical resistance	27.3 Ω	3.5 Ω	-87%
Max continuous current	1.4 A	7.5 A	+435%
Max cont. current density	4.3 A/mm ²	23 A/mm ²	+435%

F_{Fill} is assumed to be equal to 0.7. LN2 cooled magnets have an additional insulation that has a thickness T_{insul} which reduces the internal bore diameter D_b .

The flux density B_u produced by a single current loop can be calculated on its

revolution axis using the Biot-Savart law:

$$B_u(R_u, Z_u) = \frac{\mu_0 \cdot I_u}{2} \cdot \left(\frac{R_u^2}{R_u^2 + Z_u^2} \right)^{\frac{3}{2}}, \quad (2.3)$$

where R_u is the radius of the loop and Z_u is the distance along the axis between the calculation point and the center of the loop. The axial flux density created by a single finite EM is obtained by integrating this equation over the EM cross section:

$$\begin{aligned} B_e(R_e, Z_e) &= \frac{J\mu_0 F_{\text{Fill}}}{2} \int_{Z_e - T_z/2}^{Z_e + T_z/2} \int_{R_e - T_r}^{R_e} \left(\frac{R_u^2}{R_u^2 + Z_u^2} \right)^{\frac{3}{2}} dR_u dZ_u \\ &= \frac{J\mu_0 F_{\text{Fill}}}{8} \left((T_z + 2Z_e) \left(\sqrt{4R_e^2 + (T_z + 2Z_e)^2} - \sqrt{4(R_e - T_r)^2 + (T_z + 2Z_e)^2} \right) \right. \\ &\quad \left. + (T_z - 2Z_e) \left(\sqrt{4R_e^2 + (T_z - 2Z_e)^2} - \sqrt{4(R_e - T_r)^2 + (T_z - 2Z_e)^2} \right) \right), \end{aligned} \quad (2.4)$$

where R_e is the external radius of the coil, Z_e is the distance along the axis between the calculation point and the center of the coil, and J is the current density inside the copper wire. The quantity $J \cdot F_{\text{Fill}}$ is the current density averaged over the winding $T_z \times T_r$ cross section. The magnetic gradient G_e is calculated by the derivative of this equation with respect to Z_e :

$$G_e = \frac{dB_e}{dZ_e}. \quad (2.5)$$

The total power P_e dissipated inside the EM can be computed with:

$$P_e = \iiint_V F_{\text{Fill}} \cdot \rho \cdot J^2 dV, \quad (2.6)$$

over the volume V :

$$V = \pi \left(2R_e (R_e - T_{\text{insul}} - D_b) - (R_e - T_{\text{insul}} - D_b)^2 \right). \quad (2.7)$$

These equations were implemented in MATLAB with $T_z = T_r$. The function `fminsearch` was used to inverse this equation and find the value of T_z that produces the desired gradient G_e for a given R_e and Z_e .

Fig. 2.6 presents simulation results obtained using equations 2.3 to 2.6. Plot (a) graphs the EM winding volume as a function of its external diameter. The red curves correspond to magnetic assemblies able to produce a gradient strength of 20 mT/m at the system center, while the blue curves correspond to magnetic assemblies able to produce a gradient strength of 45 mT/m at the system center.. The value of T_z and therefore the volume of the winding changes along these curves to produce the desired gradient strength.

Black curves have been added to locate the functioning points for a human-size system. They represent systems that have a 0.7 m bore diameter D_b (similar to the bore diameters of MRI scanners). Dashed lines are plotted for an air cooled magnet while solid lines are for EM cooled with LN2.

To summarize, colored curved show systems that are able to produce a given gradient (20 mT/m for red curves and 45 mT/m for blue curves). The value of D_b is changing along these curves. Black curves represent systems that have D_b values of 0.7 m. The produced gradient strength is changing along these curves. The intersections of the black and colored curves represent functioning points of systems able to produce a given gradient strength with a D_b value of 0.7 m. Plot (b) in Fig. 2.6 is similar to plot (a) except that the results are presented in terms of power consumption. These data were obtained from the results presented in plot (a) and calculated using eq. 2.6.

Results show that the windings of LN2 cooled systems are always smaller than air cooled windings. They also always use less power. A human-size system producing 45 mT/m would require EMs with a volume of 0.0117 m³ and 0.0585 m³ for LN2 and air-cooled EM respectively. Their power consumptions are respectively 17.2 kW and 8.56 kW. The use of LN2 therefore allows a reduction of 80% of the winding volume and a decrease of 50% of the power consumption.

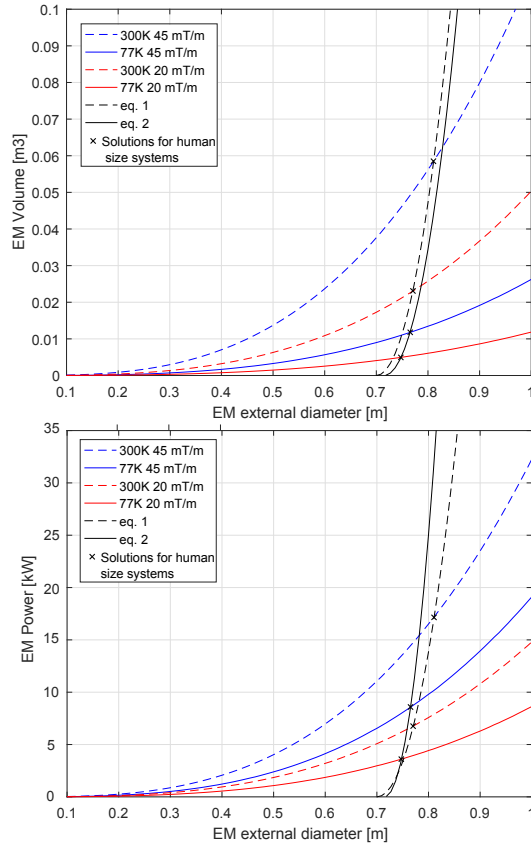


Figure 2.6: Plot of the winding volume (a) and power consumption (b) of air-cooled (300K) and LN2-cooled (77K) EMs.

2.4 Inverse Magnetics

This section analyzes 3D manipulation of a single robot having a magnetization \mathbf{m} . The magnetic manipulator is composed of six EM controlled by independent current sources. The total magnetic field is the sum of the field produced by each coil. This section calculates the coil current values to produce the desired force and torque on the robot or the desired force and magnetic field orientation.

2.4.1 Forward problem

To simplify analysis, we first solve the *forward problem* which computes the force and flux density or force and torque using the coil currents.

The system has six EMs, numerated from 1 to 6. The magnetic flux density $B_{k(\mathbf{P})}$ produced by EM number k at location \mathbf{P} can be calculated using

$$\mathbf{B}_{k(\mathbf{P})} = \begin{bmatrix} B_{kx} \\ B_{ky} \\ B_{kz} \end{bmatrix} = \tilde{\mathbf{B}}_{k(\mathbf{P})} \cdot I_k = \begin{bmatrix} \tilde{B}_{kx(\mathbf{P})} \\ \tilde{B}_{ky(\mathbf{P})} \\ \tilde{B}_{kz(\mathbf{P})} \end{bmatrix} \cdot I_k, \quad (2.8)$$

where I_k is the current in the magnet and $\mathbf{B}_{k(\mathbf{P})}$ is a function that depends on the geometry of the system and the position of the magnet. The function $\mathbf{B}_{k(\mathbf{P})}$ is computed assuming that the coils are equivalent to current loops. The flux density produced by a current loop is calculated using the semi-analytical equations presented in [15]. The flux density produced by the complete system, $\mathbf{B}(\mathbf{P})$, can be computed by summing the field produced by each magnet as

$$\mathbf{B}(\mathbf{P}) = \left(\tilde{\mathbf{B}}_{1(\mathbf{P})} + \tilde{\mathbf{B}}_{2(\mathbf{P})} + \tilde{\mathbf{B}}_{3(\mathbf{P})} + \tilde{\mathbf{B}}_{4(\mathbf{P})} + \tilde{\mathbf{B}}_{5(\mathbf{P})} + \tilde{\mathbf{B}}_{6(\mathbf{P})} \right) \mathbf{I}, \quad (2.9)$$

where \mathbf{I} is a vector containing the current of each coil.

It is now necessary to define three new vectors:

$$\tilde{\mathbf{B}}_x(\mathbf{P}) = \left[\tilde{B}_{1x(\mathbf{P})} \tilde{B}_{2x(\mathbf{P})} \tilde{B}_{3x(\mathbf{P})} \tilde{B}_{4x(\mathbf{P})} \tilde{B}_{5x(\mathbf{P})} \tilde{B}_{6x(\mathbf{P})} \right], \quad (2.10)$$

$$\tilde{\mathbf{B}}_y(\mathbf{P}) = \left[\tilde{B}_{1y(\mathbf{P})} \tilde{B}_{2y(\mathbf{P})} \tilde{B}_{3y(\mathbf{P})} \tilde{B}_{4y(\mathbf{P})} \tilde{B}_{5y(\mathbf{P})} \tilde{B}_{6y(\mathbf{P})} \right], \text{ and} \quad (2.11)$$

$$\tilde{\mathbf{B}}_z(\mathbf{P}) = \left[\tilde{B}_{1z(\mathbf{P})} \tilde{B}_{2z(\mathbf{P})} \tilde{B}_{3z(\mathbf{P})} \tilde{B}_{4z(\mathbf{P})} \tilde{B}_{5z(\mathbf{P})} \tilde{B}_{6z(\mathbf{P})} \right]. \quad (2.12)$$

Equation 2.9 can be re-written as

$$\mathbf{B}(\mathbf{P}) = \begin{bmatrix} \tilde{\mathbf{B}}_x(\mathbf{P}) \\ \tilde{\mathbf{B}}_y(\mathbf{P}) \\ \tilde{\mathbf{B}}_z(\mathbf{P}) \end{bmatrix} \cdot \mathbf{I}. \quad (2.13)$$

The force \mathbf{F} is calculated with:

$$\mathbf{F} = \begin{bmatrix} F_x(\mathbf{P}) \\ F_y(\mathbf{P}) \\ F_z(\mathbf{P}) \end{bmatrix} = \nabla \cdot (\mathbf{m} \cdot \mathbf{B}(\mathbf{P})), \quad (2.14)$$

which can be re-written as:

$$\mathbf{F} = \begin{bmatrix} m_x \cdot \frac{\partial \tilde{\mathbf{B}}_x(\mathbf{P})}{\partial x} + m_y \cdot \frac{\partial \tilde{\mathbf{B}}_y(\mathbf{P})}{\partial x} + m_z \cdot \frac{\partial \tilde{\mathbf{B}}_z(\mathbf{P})}{\partial x} \\ m_x \cdot \frac{\partial \tilde{\mathbf{B}}_x(\mathbf{P})}{\partial y} + m_y \cdot \frac{\partial \tilde{\mathbf{B}}_y(\mathbf{P})}{\partial y} + m_z \cdot \frac{\partial \tilde{\mathbf{B}}_z(\mathbf{P})}{\partial y} \\ m_x \cdot \frac{\partial \tilde{\mathbf{B}}_x(\mathbf{P})}{\partial z} + m_y \cdot \frac{\partial \tilde{\mathbf{B}}_y(\mathbf{P})}{\partial z} + m_z \cdot \frac{\partial \tilde{\mathbf{B}}_z(\mathbf{P})}{\partial z} \end{bmatrix} \cdot \mathbf{I}. \quad (2.15)$$

The torque \mathbf{T} is calculated with:

$$\mathbf{T} = \begin{bmatrix} T_x(\mathbf{P}) \\ T_y(\mathbf{P}) \\ T_z(\mathbf{P}) \end{bmatrix} = \mathbf{m} \times \mathbf{B}, \quad (2.16)$$

which can be re-written as

$$\mathbf{T} = \begin{bmatrix} m_y \cdot \tilde{\mathbf{B}}_z(\mathbf{P}) - m_z \cdot \tilde{\mathbf{B}}_y(\mathbf{P}) \\ m_z \cdot \tilde{\mathbf{B}}_x(\mathbf{P}) - m_x \cdot \tilde{\mathbf{B}}_z(\mathbf{P}) \\ m_x \cdot \tilde{\mathbf{B}}_y(\mathbf{P}) - m_y \cdot \tilde{\mathbf{B}}_x(\mathbf{P}) \end{bmatrix} \cdot \mathbf{I}. \quad (2.17)$$

2.4.2 Inverse problem

Two inverse methods are studied. The first one aims at controlling the flux density and the force applied on the robot using the actuation matrix \mathbf{A}_0 :

$$\mathbf{A}_0 = \begin{bmatrix} \tilde{\mathbf{B}}_x(\mathbf{P}) \\ \tilde{\mathbf{B}}_y(\mathbf{P}) \\ \tilde{\mathbf{B}}_z(\mathbf{P}) \\ m_x \cdot \frac{\partial \tilde{\mathbf{B}}_x(\mathbf{P})}{\partial x} + m_y \cdot \frac{\partial \tilde{\mathbf{B}}_y(\mathbf{P})}{\partial x} + m_z \cdot \frac{\partial \tilde{\mathbf{B}}_z(\mathbf{P})}{\partial x} \\ m_x \cdot \frac{\partial \tilde{\mathbf{B}}_x(\mathbf{P})}{\partial y} + m_y \cdot \frac{\partial \tilde{\mathbf{B}}_y(\mathbf{P})}{\partial y} + m_z \cdot \frac{\partial \tilde{\mathbf{B}}_z(\mathbf{P})}{\partial y} \\ m_x \cdot \frac{\partial \tilde{\mathbf{B}}_x(\mathbf{P})}{\partial z} + m_y \cdot \frac{\partial \tilde{\mathbf{B}}_y(\mathbf{P})}{\partial z} + m_z \cdot \frac{\partial \tilde{\mathbf{B}}_z(\mathbf{P})}{\partial z} \end{bmatrix}. \quad (2.18)$$

The force and flux density are equal to:

$$\begin{bmatrix} \mathbf{B} \\ \mathbf{F} \end{bmatrix} = \mathbf{A}_0 \cdot \mathbf{I}. \quad (2.19)$$

\mathbf{A}_0 is a square matrix and can be inverted provided that it is not singular. The current \mathbf{I} is calculated with:

$$\mathbf{I} = \mathbf{A}_0^{-1} \cdot \begin{bmatrix} \mathbf{B} \\ \mathbf{F} \end{bmatrix}. \quad (2.20)$$

The second method controls the force and torque applied on the robot using the actuation matrix \mathbf{A}_1

$$\mathbf{A}_1 = \begin{bmatrix} m_y \cdot \tilde{\mathbf{B}}_z(\mathbf{P}) - m_z \cdot \tilde{\mathbf{B}}_y(\mathbf{P}) \\ m_z \cdot \tilde{\mathbf{B}}_x(\mathbf{P}) - m_x \cdot \tilde{\mathbf{B}}_z(\mathbf{P}) \\ m_x \cdot \tilde{\mathbf{B}}_y(\mathbf{P}) - m_y \cdot \tilde{\mathbf{B}}_x(\mathbf{P}) \\ m_x \cdot \frac{\partial \tilde{\mathbf{B}}_x(\mathbf{P})}{\partial x} + m_y \cdot \frac{\partial \tilde{\mathbf{B}}_y(\mathbf{P})}{\partial x} + m_z \cdot \frac{\partial \tilde{\mathbf{B}}_z(\mathbf{P})}{\partial x} \\ m_x \cdot \frac{\partial \tilde{\mathbf{B}}_x(\mathbf{P})}{\partial y} + m_y \cdot \frac{\partial \tilde{\mathbf{B}}_y(\mathbf{P})}{\partial y} + m_z \cdot \frac{\partial \tilde{\mathbf{B}}_z(\mathbf{P})}{\partial y} \\ m_x \cdot \frac{\partial \tilde{\mathbf{B}}_x(\mathbf{P})}{\partial z} + m_y \cdot \frac{\partial \tilde{\mathbf{B}}_y(\mathbf{P})}{\partial z} + m_z \cdot \frac{\partial \tilde{\mathbf{B}}_z(\mathbf{P})}{\partial z} \end{bmatrix}. \quad (2.21)$$

The torque and force are equal to:

$$\begin{bmatrix} \mathbf{T} \\ \mathbf{F} \end{bmatrix} = \mathbf{A}_1 \cdot \mathbf{I}. \quad (2.22)$$

\mathbf{A}_1 is a square matrix and can be inverted provided that it is not singular. The current \mathbf{I} is calculated with:

$$\mathbf{I} = \mathbf{A}_1^{-1} \cdot \begin{bmatrix} \mathbf{T} \\ \mathbf{F} \end{bmatrix}. \quad (2.23)$$

2.5 Trajectory control

Equation 2.19 shows that \mathbf{F} is decoupled from \mathbf{B} and \mathbf{T} . The control of \mathbf{B} enables the control of the orientation of the robot. The robot can be assumed to be oriented along the magnetic field direction, as in [13]. The magnitude of the flux density $|\mathbf{B}|$ is set to a constant value and the individual components are calculated to obtain the desired field orientation. Another alternative is to use eq. 2.23 to control the torque directly.

The trajectory is controlled using the controller presented in Fig. 2.3(b). It uses a nested control structure. The inner PID control loop regulates velocity, which is limited by a saturation function to avoid excessive speeds and instabilities. The outer loop generates a velocity setpoint.

The trajectory is defined by the user as a set of viapoints and the corresponding desired velocities V_t . The outer loop first searches for the point of the trajectory that is the closest to the robot position and determines V_t . An additional velocity component V_s is added to this value to steer the robot toward the trajectory centerline.

When the calculated current is above the maximum value (I_{\max} is the maximum current the power supplies can generate) the vector \mathbf{I} is scaled down so that the largest element of \mathbf{I} is equal to I_{\max} . This reduces the force and flux density values applied on the robot, but has the advantage of keeping the correct field and force orientation.

2.6 Singularities analysis for a 3-DOF robot

As explained in Section 2.5, the orientation of the robot can be controlled using two different methods. The first one uses actuation matrix \mathbf{A}_0 and allows applying a desired flux density vector \mathbf{B} and a force \mathbf{F} to the robot. The second uses actuation matrix \mathbf{A}_1 and allows applying a desired torque \mathbf{T} and a force \mathbf{F} to the robot.

When expressed in the manipulator coordinate system (x, y, z) , \mathbf{A}_1 is square. However, the robot is symmetric around its revolution axis d and therefore no torque can be applied on the d axis. Defining a new coordinate system (d, q, w) allows removing one dimension from \mathbf{A}_1 (i.e. \mathbf{A}_1 has a size 5×6 when expressed in the (d, q, w) coordinate system). The system is therefore underdetermined and the least square solution is calculated using

$$\mathbf{I} = \mathbf{A}_1^T (\mathbf{A}_1 \cdot \mathbf{A}_1^T)^{-1} \cdot \begin{bmatrix} \mathbf{T} \\ \mathbf{F} \end{bmatrix}. \quad (2.24)$$

The actuation matrices \mathbf{A}_0 and \mathbf{A}_1 are functions of the magnetic manipulator geometry and the robot pose.

The effect of singularities was studied for a 2D–3DOF control. The magnet is

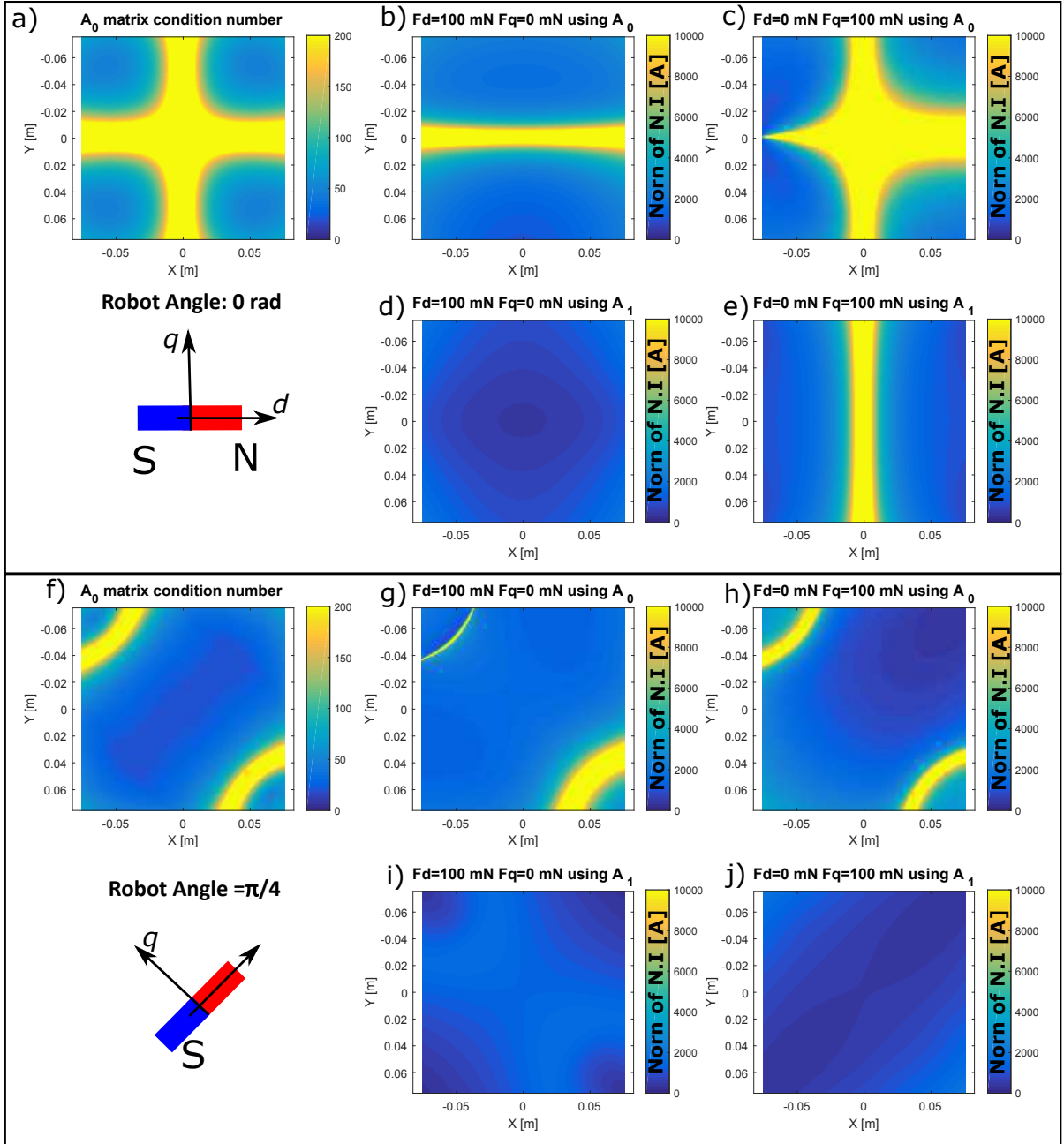


Figure 2.7: Map of the conditioning of the actuation matrix \mathbf{A}_0 for (a) $\theta = 0$ and (f) $\theta = \pi/4$. Map of the norm of the total current needed to produce a force of 100 mN along the d axis (b, d, g and i) and along the q axis (c, e, h and j).

horizontally placed on a flat surface corresponding to the x - y plane. The robot is able to move along x and y and rotate around the z -axis.

A 4×4 \mathbf{A}_0 and a 4×3 \mathbf{A}_1 actuation matrices can be calculated for each robot position and angle. The map of the conditioning of the \mathbf{A}_0 matrix is shown in Fig. 2.7(a) and (f). On this figure is also presented the norm of the total current $N \cdot \mathbf{I}$ required to produce a force of 100 mN along the d -axis (central-column) and q -axis (right-column). Plots b, c, d and e are plotted for $\theta = 0$ and plots g, h, i and j are plotted for $\theta = \pi/4$. Plots b, c, g and h were calculated using \mathbf{A}_0 and plots d, e, i and j were calculated using \mathbf{A}_1 .

For $\theta = 0$, \mathbf{A}_0 has two singularity lines on the x and y axis. For $\theta = \pi/4$ singularities take a rounded shape and are located on two opposite angles of the workspace. No solution is available when the matrix is singular. The singularities are situated on infinitely thin lines, but the system is ill-conditioned near the singularity lines. A large condition number produces a large magnitude for the \mathbf{I} vector. The capabilities of the power supplies limit the maximum current and when the condition number becomes too large, the current saturates. This saturation decreases control authority over the robot in these regions.

The norm of the total current $N \cdot \mathbf{I}$ needed to produce a force of 100 mN along the d and q axis was calculated as a function of the robot position and angle. Plots b, c, e and f of Fig. 2.7 present these results. When using the \mathbf{A}_0 matrix, there are areas where the current becomes larger than 10,000 A close to the singularities when the force is generated along the d axis as well as when the force is generated along the q axis. When using \mathbf{A}_1 , these large current densities are present only when a force is generated along the q axis. When the force is produced along the d axis, the current always stays within relatively small values. This observation is valid for any robot orientation.

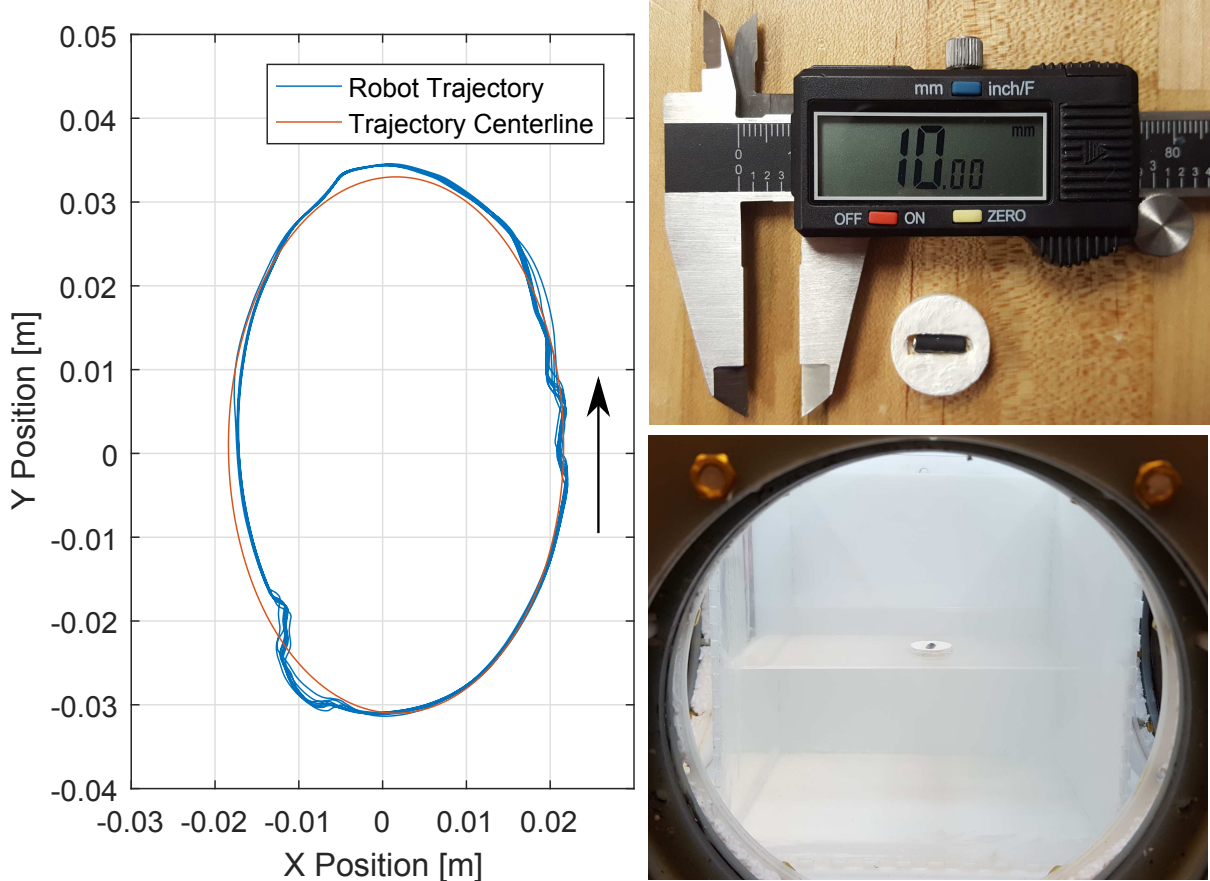


Figure 2.8: Plot of the trajectory of the robot obtained experimentally. For this dataset, the robot completed the path ten times. The robot and the workspace are shown at right.

2.7 Experimental Results

The control of the velocity and orientation of a NdFeB permanent magnet in a 2D plane described in Section 2.5 was implemented and tested using the \mathbf{A}_1 actuation matrix. As shown in Section 2.6 it is preferable to apply the force along the magnetization axis of the robot (d -axis). The program was therefore configured to orient the robot magnetization in the same direction as the applied force. This allows minimizing the value of the force applied along the q axis and therefore improve stability by avoiding current saturations. The permanent magnet was cylindrical, with a diameter of 2.5 mm and a length of 10 mm. It was encapsulated in a black shrink tube to facilitate computer vision tracking. The magnet was then attached horizontally on a Styrofoam disk having

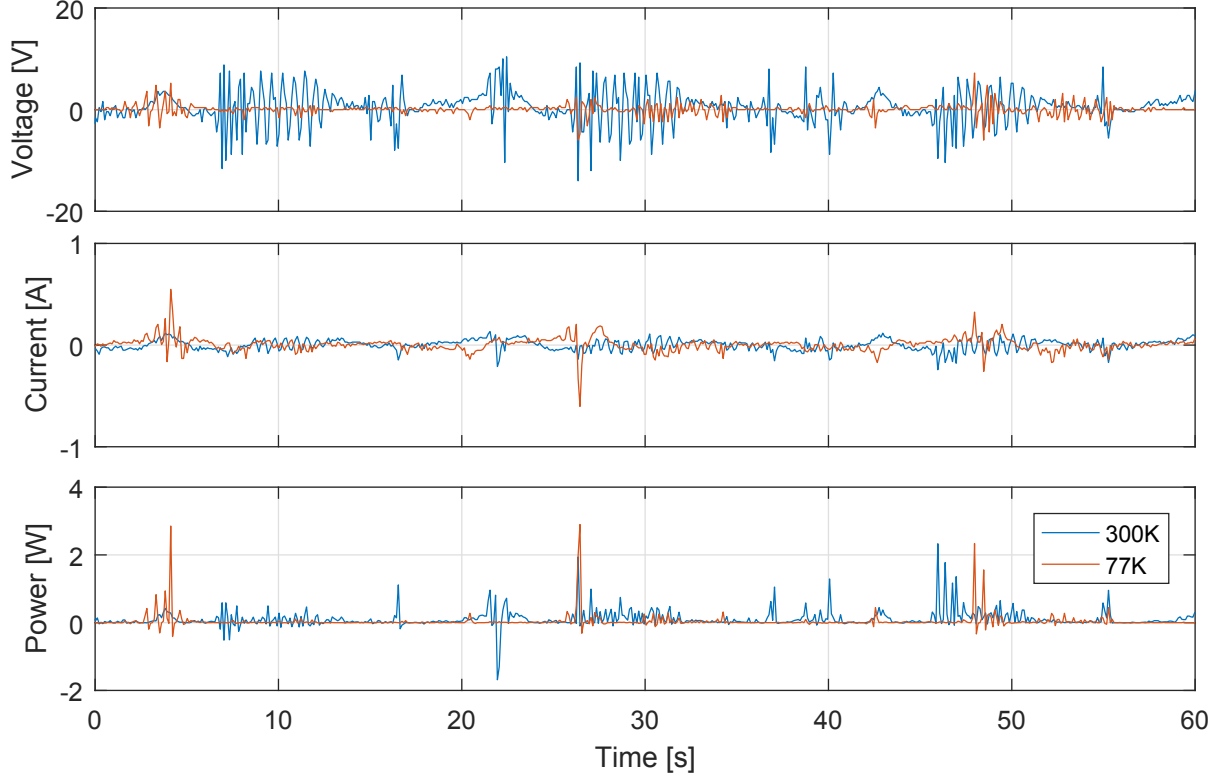


Figure 2.9: Voltage, current, and power used during robot navigation. The curves show 60 seconds of data, which correspond to the robot completing the trajectory in Fig. 2.8 three times.

a diameter of 18 mm and a thickness of 6 mm. Pictures of the robot are shown in Fig. 2.8.

A robot navigating inside fluid-filled cavities of the human body may be designed to have neutral buoyancy to reduce the amount of force needed. To simulate neutral buoyancy in this 2D control experiment, the magnet-Styrofoam assembly floated at the surface of a water-filled tank. The magnet was able to move freely in the x and y directions as well as rotate around the z axis.

The method from Section 2.5 was used with the \mathbf{A}_1 actuation matrix from (2.21). The trajectory was an ellipse having a major axis of 63 mm and a minor axis of 40 mm.

Test were performed with and without LN2 cooling. The trajectory obtained experimentally without LN2 is presented in Fig. 2.8. For these plots, the robot followed the trajectory ten times. Trajectories obtained with LN2 cooling are similar. The robot

was stable during the navigation, but small deviation from the centerline were observed at several locations.

The current and voltage applied on the $-x$ EM was recorded during one minute for both cooling methods. The instantaneous power was calculated from these data and the results are presented in Fig. 2.9. The average power used for the air cooled case is equal to 0.218 W whereas it is only equal to 0.037 W when magnets are cooled with LN2. This decrease of average power consumption is enabled by the decrease of copper electrical resistivity when cooled at 77K and produces a decrease of the applied voltage as shown in Fig. 2.9(a). The parameters of the controller were not changed between the tests, however, the peak power is increased when LN2 is added. This behavior could be explained by an increase of the current regulation dynamics performed by the power supply when the electrical resistance of the EM is decreased by the cooling.

The power used was low because the floating robot required little force. Applications that navigate against flow or perform surgery require larger forces and correspondingly more power.

2.8 Conclusion and Future Works

This paper presented a magnetic manipulator using EM cooled with LN2. Liquid nitrogen cooling allows increasing the current circulating inside an EM up to 435%. This cooling enables reducing the size of the EM to produce a given magnetic field. The required electromagnets to achieve a given flux density are cheaper to build, and the complete system is more compact.

A desktop-size prototype was built and tested. The robot, a cylindrical permanent magnet, was manipulated on a 2D plane. Three DOF were controlled: the orientation and the x and y positions.

The system was not designed to produce a uniform magnetic field. Instead, inverse

magnetic calculations account for field non-uniformities. The current inside each coil is computed to generate the desired force on the robot and produce the desired field orientation.

The system's matrix conditioning was analyzed. The matrix is sometimes ill-conditioned, depending on the position and orientation of the robot. Issues with ill conditioning can be avoided by controlling the torque directly and avoiding the production of forces along the axis perpendicular to the robot magnetization.

More control inputs can be added to improve the controllability of the robot. A possibility is to use additional EM, as in [13] where eight EMs were used to control a five DOF robot, but using additional EMs makes the system more complicated and expensive to build.

Future study will focus on the addition of a high-frequency component to the magnetic field to increase the controllability of the robot. A permanent magnet could be encapsulated in a conductive shell such as copper. If the robot is electrically conductive, the AC field would induce currents in it, and generate an additional torque as in an induction electric motor. This AC magnetic field could also be used to control resonating magnetic actuators as in [16]. Finally, the controller could include a temperature management feature that calculates the heat dissipated in the windings and avoids overheating by preventively reducing power.

Chapter 3

Two-Body Magnetic Manipulation with Global Inputs

This chapter is based on a journal submission with Shiva Shahrokhi, Jingang Shi, Benedict Isichei, and Aaron T. Becker. The author’s contribution was focused on creating the Intestine Phantom Model and Bovine Intestine model for physical implementation of the algorithm, along with obtaining experimental results. This work was supported by the National Science Foundation under Grant No. [IIS-1553063] and [IIS-1619278].

Steered particles offer a method for targeted therapy, interventions, and drug delivery in regions inaccessible by large robots. As stated in the previous chapter, magnetic actuation has the benefits of requiring no tethers, being able to operate from a distance, and in some cases allows imaging for feedback (e.g. MRI). This paper investigates particle control with uniform magnetic gradients (the same force is applied everywhere in the workspace). Given three orthogonal magnetic fields, steering one particle in 3D is trivial. Adding additional particles to steer makes the system underactuated because there are more states than control inputs. However, the walls of in vivo and artificial environments often have surface roughness such that the particles do not move unless actuation pulls them away from the wall. It has been shown that the individual 2D position of two particles is controllable in a square workspace with non-slip wall contact [17]. Because in vivo environments are usually not square, this paper extends the previous work to all convex workspaces, and then implements the algorithms using a hardware setup inspired by the gastrointestinal tract.

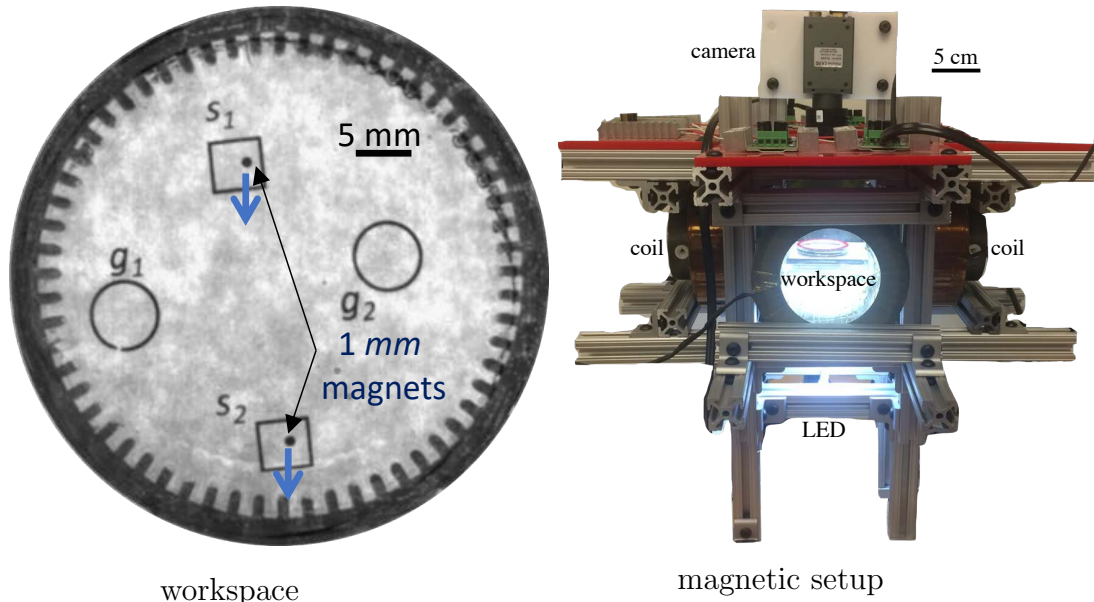
3.1 Introduction

Particle swarms propelled by a uniform field, where each particle receives the same control input, are common in applied mathematics, biology, and computer graphics [18, 19, 20].

The small size of these robots makes it difficult to perform onboard computation. Instead, these robots are often controlled by a broadcast signal. The tiny robots themselves are often just rigid bodies, and it may be more accurate to define the robot as the *system* that consists of particles, a uniform control field, and sensing. Such systems are severely underactuated, having 2 degrees of freedom in the shared planar control input, but $2n$ degrees of freedom for the n -particle swarm. Techniques are needed that can handle this underactuation.

Positioning is a foundational capability for a robotic system, e.g., placement of brachytherapy seeds. In [21], it was shown that the 2D position of each particle in such a swarm is controllable if the workspace contains a single obstacle the size of one particle. However, requiring a single, small, rigid obstacle suspended in the middle of the workspace is often an unreasonable constraint, especially in 3D. This paper relaxes that constraint, and provides position control algorithms that only require non-slip wall contacts. The particles in contact with the boundaries are assumed to have zero velocity if the uniform control input pushes the particle into the wall.

This paper is an elaboration of preliminary work in a conference paper [17] which considered only square workspaces. This work extends the analysis to convex workspaces and also implements the algorithms using a hardware setup inspired by the anatomy of the gastrointestinal tract.



workspace
magnetic setup
Figure 3.1: Workspace and magnetic setup for an experiment to position particles that receive the same control inputs, but cannot move while a control input pushes them into a boundary.

3.2 Related Work

Controlling the *shape*, or relative positions, of a swarm of robots is a key ability for a range of applications. Correspondingly, it has been studied from a control-theoretic perspective in both centralized and decentralized approaches. For examples of each, see the centralized virtual leaders in [22], and the gradient-based decentralized controllers using control-Lyapunov functions in [23]. However, these approaches assume a level of intelligence and autonomy in individual robots that exceeds the capabilities of many systems, including current micro- and nano-robots. Current micro- and nano-robots, such as those in [24, 25, 26] lack onboard computation.

This paper focuses on centralized techniques that apply the same control input to both particles. Precision control requires breaking the symmetry caused by the uniform input. Symmetry can be broken using particles that respond differently to the uniform control signal, either through agent-agent reactions [27], or engineered inhomogeneity [28, 29, 30]. The magnetic gradients of MRI scanners are *uniform*, meaning the same

force is applied everywhere in the workspace[31]. This work assumes a uniform control with homogenous particles, as in [21], and breaks the control symmetry using obstacles in the workspace.

Alternative techniques rely on non-uniform inputs, such as artificial force-fields. Applications have included techniques to design shear forces for sensorless manipulation of a single object by [32]. [33] demonstrated a collection of 2D force fields generated by six degree-of-freedom vibration inputs to a rigid plate. These force fields, including shear forces, could be used as a set of primitives for motion control to steer the formation of multiple objects.

Similarly, much recent work in magnet control has focused on exploiting inhomogeneities in the magnetic field to control multiple micro particles using gradient-based pulling [34, 35]. Unfortunately, using large-scale external magnetic fields makes it challenging to independently control more than one microrobot unless the distance between the electromagnetic coils is at the same length scales as the robot workspace [36, 35, 34]. In contrast, this paper requires only a controllable constant gradient in orthogonal directions to position the particles.

If a control input causes the particles to collide with obstacles at different times, inverting the control input does not undo the action. Due to this lack of time-reversibility, techniques that require a bidirectional graph, e.g. PRM [37] and RRT* [38] are not suitable. Instead, this paper employs a greedy search strategy.

3.3 Theory

In the absence of obstacles, uniform inputs move a swarm identically. Independent control requires breaking this symmetry. The following sections examine using non-slip boundary contacts to break the symmetry caused by uniform inputs. The developed algorithms rely on holding one particle stationary by pushing it into the boundary while

moving the other particle. The section begins with a boundary interaction model in subsection 3.3.1.

3.3.1 Boundary Interaction Model

The system dynamics represent particle swarms in low-Reynolds number environments, where viscosity dominates inertial forces and so velocity is proportional to input force [39]. In this regime, the input force command $\mathbf{u}(t)$ controls the velocity of the particles. If the i^{th} particle has position $\mathbf{x}_i(t)$ and velocity $\dot{\mathbf{x}}_i(t)$, the following system model is assumed:

$$\dot{\mathbf{x}}_i(t) = \mathbf{u}(t) + F(\mathbf{x}_i(t), \mathbf{u}(t)), \quad i \in [1, n]. \quad (3.1)$$

$$F(\mathbf{x}_i(t), \mathbf{u}(t)) = \begin{cases} -\mathbf{u}(t) & \mathbf{x}_i(t) \in \text{boundary and} \\ & \mathbf{N}(\text{boundary}_{\mathbf{x}_i(t)}) \cdot \mathbf{u}(t) \leq 0 \\ 0 & \text{else.} \end{cases}$$

Here $F(\mathbf{x}_i(t), \mathbf{u}(t))$ is the frictional force provided by the boundary, and $\mathbf{N}(\text{boundary}_{\mathbf{x}_i(t)})$ is the normal to the boundary at position $\mathbf{x}_i(t)$.

The same model can be generalized to particles moved by fluid flow where the vector direction of fluid flow $\mathbf{u}(t)$ controls the velocity of particles, or for a swarm of particles that move at a constant speed in a direction specified by a uniform input $\mathbf{u}(t)$ [40]. As in this model, fluid flowing in a pipe has zero velocity along the boundary. Similar mechanical systems exist at larger scales, e.g. all tumblers of a combination lock move uniformly unless obstructed by an obstacle. The control problem is to design the control inputs $\mathbf{u}(t)$ to deliver two particles to goal positions.

3.4 Experimental Results

To demonstrate the developed algorithm experimentally, several tests were performed. Each used the same magnetic setup shown in Fig. 3.1. Two different intestine

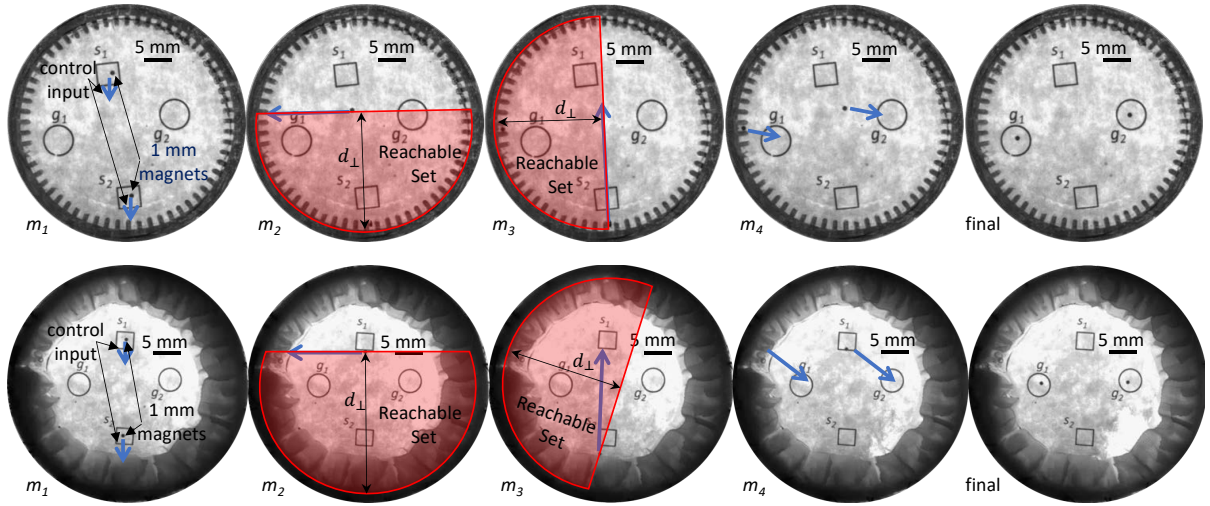


Figure 3.2: Frames showing particle positions before and after control inputs. Top row: small intestine phantom. Bottom row: cow stomach tissue.

models were employed, the first a 3D-printed cross-section representation of a small intestine, and the second a cross-section of a bovine stomach.

3.4.1 Magnetic Manipulation Setup

The magnetic manipulation system has two pairs of electromagnetic coils, each with iron cores at their centers, and arranged orthogonal to each other. The iron core at the center of each coil concentrates the magnetic field towards the workspace. An Arduino and four SyRen regenerative motor drivers were used for control inputs to the coils. Finally, a FOculus F0134SB 659 x 494 pixel camera was attached to the top of the system, focusing on the workspace which was backlit by a 15 W LED light strip.

To obtain experimental data, the test samples (the phantom intestine model and the bovine cross section) were placed in laser-cut acrylic discs and then immersed in corn syrup. Corn syrup was used to increase the viscosity to 12000 cP for the experiments. Spherical 1 mm magnets (supermagnetman #SP0100-50) were used as the test particles. Our experimental setup did not perfectly implement the system dynamics in (3.1). In particular, the magnetic field in this setup is only approximately uniform. The magnetic

force varies in both magnitude and orientation. This non-uniformity causes the particle closer to the coil to move faster than the other particle. This phenomenon makes it easier to increase particle separation than to decrease separation, but this can be compensated because boundary collisions easily decrease the separation. Also, magnetic forces are not exactly parallel, but point toward the center of the activated coil. The developed algorithm still works despite these non-uniformities, but sometimes requires additional iterations.

3.4.2 Intestine Phantom Model

The intestine phantom model was used first and was made to mimic the geometry of an intestine and its villi. The model consists of a circular ring with an outer diameter of 50 mm, an inner diameter of 46 mm, and 60 2 mm long protrusions on its inner surface cut out of 6 mm thick acrylic to model the geometry of intestinal villi. Figure 3.2 top row shows an experiment. Starting and ending positions were printed beneath the workspace on transparency film. The developed algorithm successfully delivered the particles to goal positions in 10 out of 10 trials.

3.4.3 Bovine Stomach Cross-section

Strips of cow stomach approximately 5 mm thick were cut and sewn to acrylic cylinder and then glued to an acrylic substrate using cyanoacrylate (superglue). This assembly was then filled with corn syrup. The experiment is shown in Fig. 3.2 bottom row. The developed algorithm successfully delivered the particles to goal positions in 5 out of 5 trials.

3.5 Conclusion and Future Work

This paper presented techniques for controlling the positions of two particles using uniform inputs and non-slip boundary contacts. The paper provided algorithms for precise position control. The algorithms relied on calculating reachable sets in a 2D Δ configuration space. Hardware experiments illustrated the algorithms in ex vivo and in artificial workspaces that mimic the geometry of biological tissue.

There are several avenues for future work. This paper assumed friction was sufficient to completely stop particles in contact with the boundary. The algorithms would require retooling to handle small friction coefficients. The techniques in [17] and [21] could be applied to extend the analysis to more than two particles.

Chapter 4

Low-Cost Robot Manipulator Arms

The course Introduction to robots focuses on robotic manipulators. As a TA for this class, a series of labs using a cheap (under US \$50) robot arm kit were designed to aid students in comprehending the subject material.

The kit, as purchased, is not a robot. It is instead a device with five user-controlled motors that can be turned on or off. The main aim of these labs are to introduce the students to robotics concepts and control systems. A GUI was also implemented for lower-level students to introduce them to programming a simple robot and cultivate interest in robotics.

The labs are arranged as follows:

1. Lab 1: Assembly and familiarization
2. Lab 2: Open-loop control



Figure 4.1: The unmodified robotic arm



Figure 4.2: The parts of the robot arm before assembly

3. Lab 3: Closed-loop control with Potentiometer sensors
4. Lab 4: Closed-loop control with image processing

4.1 Lab 1: Assembly and Familiarization

For this lab, the students were tasked with assembling the robot and controlling it with its default controller. They were tasked with moving around little objects within the robot's workspace to get an idea of the robot's capabilities. By assembling the robot themselves, the students become intimately familiar with the limits of the robot, and its possible orientations. After testing the robot in its default configuration, the students are then instructed on the first stage in augmenting the robot arm—switching out the original control circuit with a custom built Printed Circuit Board (PCB).

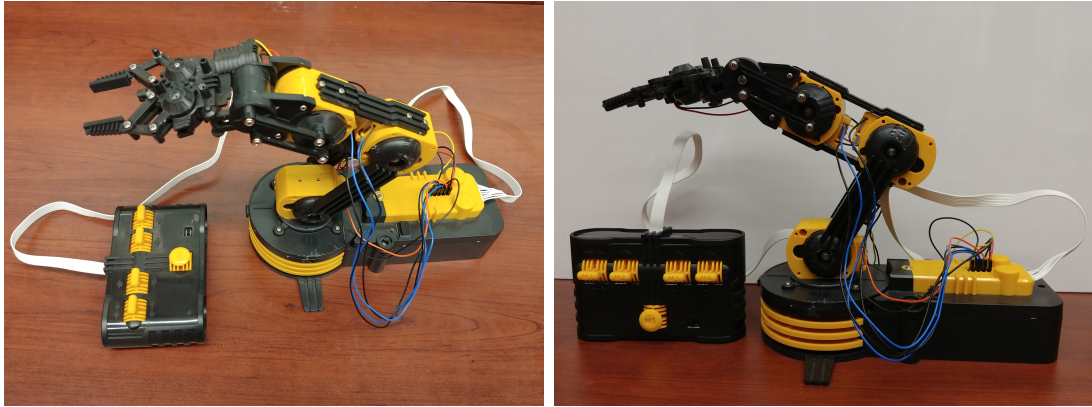


Figure 4.3: The assembled robotic arm

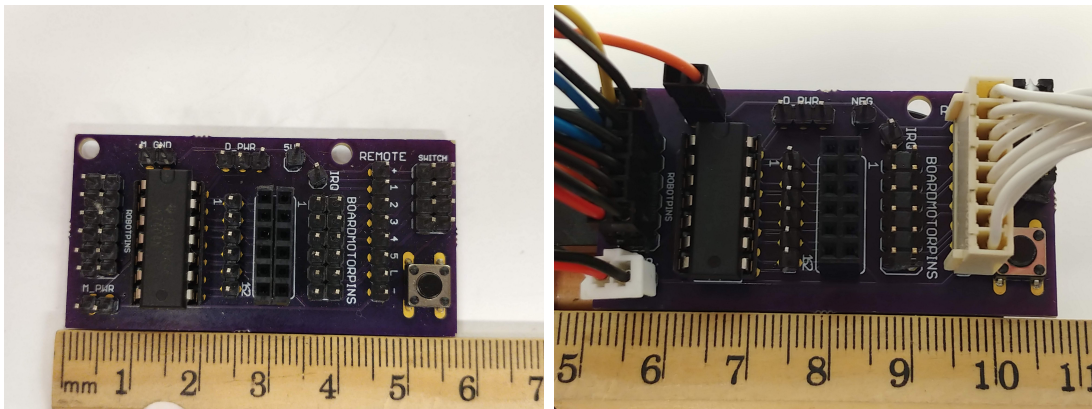


Figure 4.4: The custom PCB with initial configuration as a manual remote

4.2 Lab 2: Open-Loop Control

For this lab, the students were tasked with altering the robot to include a microprocessor for open-loop control. Using a motor driver and an Arduino microprocessor, the students were instructed on how to include a degree of automation to the robot's movements. The main aim of this project was to showcase the ease to which automation can be achieved, but also make them aware of how unreliable automation is without sensor feedback for control.

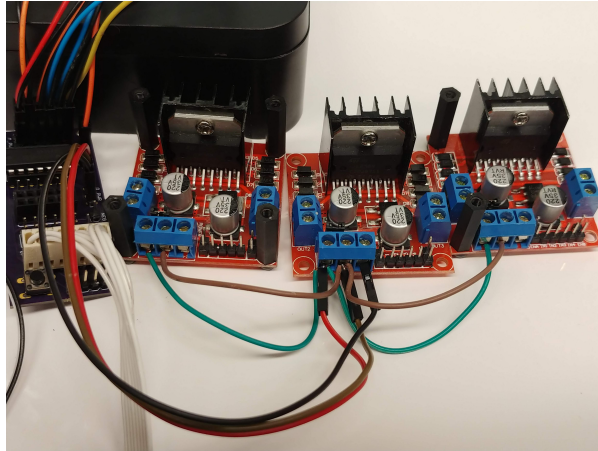


Figure 4.5: Intermediate step in assembling the arm for open-loop control

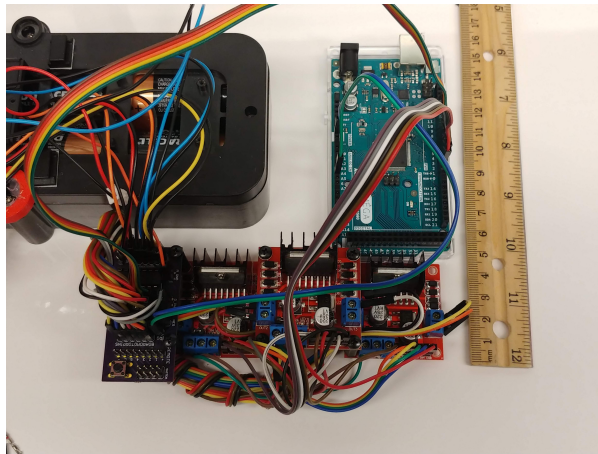


Figure 4.6: Fully connected microcontroller, motor driver and PCB boards for open-loop control

4.3 Lab 3: Closed-loop Control with Potentiometer Sensors

For this lab, the students were tasked with altering the robot further to include potentiometers to read its joint values and thus implement closed-loop control with forward kinematics. The students were provided with instructions on how to attach the potentiometers to the robot with some custom designed 3D printed parts and lasercut gears. The aim of this lab was to help students understand the importance of implementing feedback in robotics control systems, and to a certain extent, introduce them to fabrication and design.

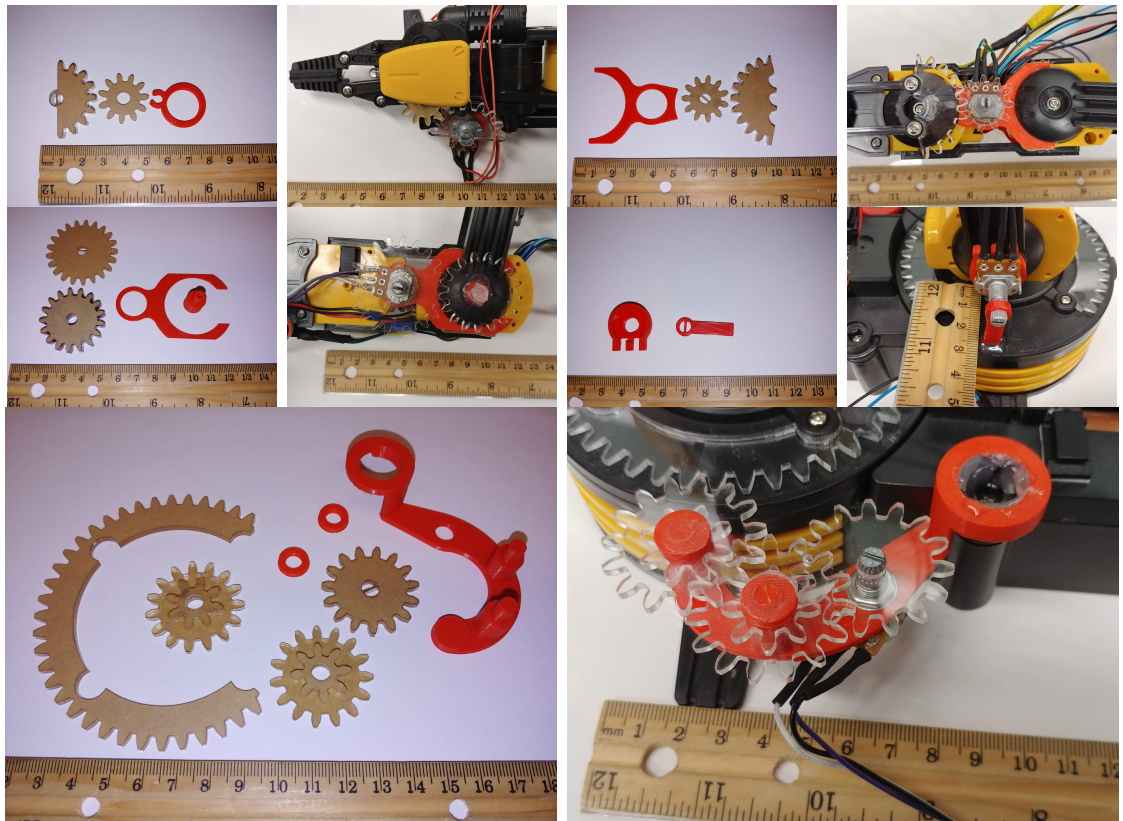


Figure 4.7: The fabricated parts, and augmented joints

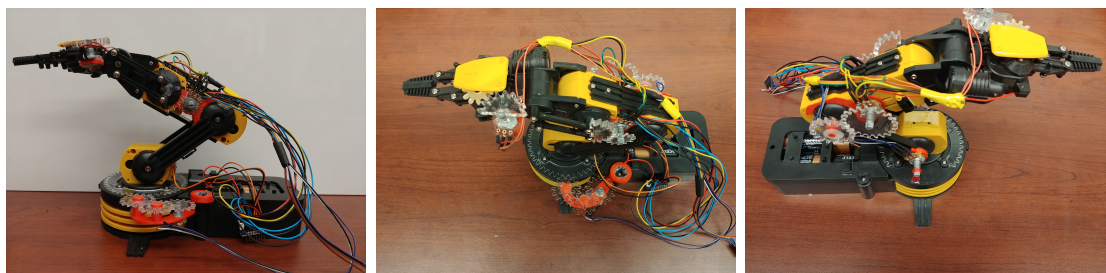


Figure 4.8: The augmented robotic arm

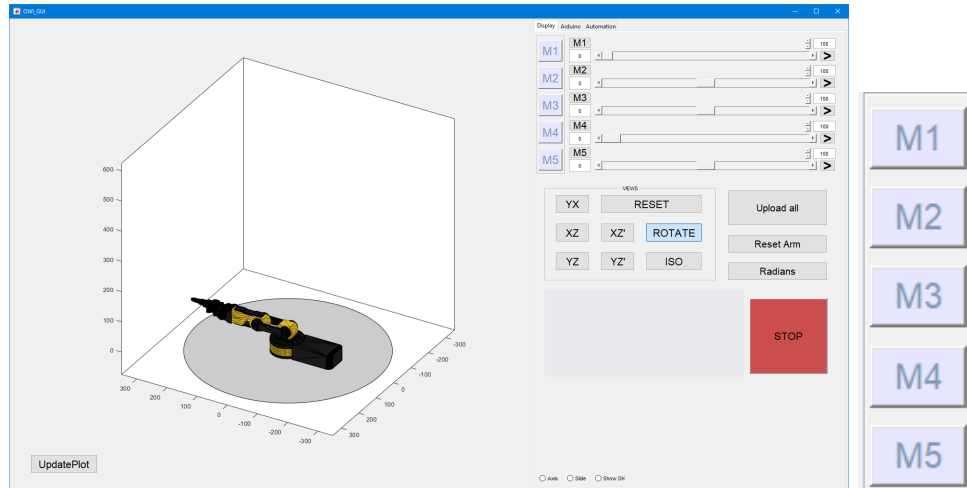


Figure 4.9: The graphical user interface, and the virtual remote control. To allow ease of access, the virtual remote is accessible from all tabs in the GUI, and can be used after the Arduino input/output pins have been set

4.4 Lab 4: Closed-loop Control with Image Processing

For this lab, the students were tasked with using camera inputs to control the robot in a simple tracking task. This illustrates closed-loop control with inverse kinematics. With this lab the students are introduced to another method of sensory feedback, and also given an introduction to image processing.

4.5 GUI

For the main introduction to robotics class, the students are assumed to know the basics of programming. For those without the skill, and for situations in which the robotic arm is to be used for outreach opportunities, a graphical user interface (GUI) was also developed for the arm. Fig 4.9 shows the default view of the GUI¹. It includes a preview screen on the left, and several tabs on the right for setup information, virtual controls, and automation.

¹<https://github.com/bisichei/owi-gui>

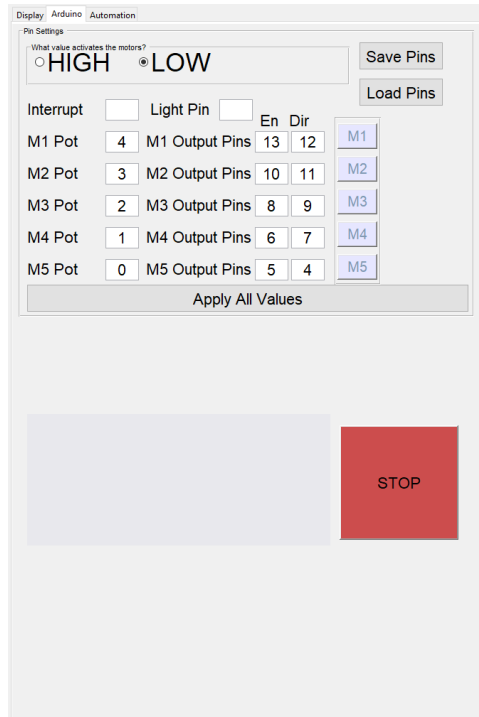


Figure 4.10: The setup tab of the user interface. The program takes the user through the steps required to configure the input/output pins, and calibrate the robot’s potentiometers

4.5.1 Configuration

In order to fully utilize the GUI, the user is first tasked with inputting a series of Arduino pin values that describe what the microprocessor’s inputs and outputs as show in Fig 4.10. After setting up the pin information, the user gains use of the virtual remote control of the GUI. Following this setup, they are then tasked with calibrating the robot’s potentiometer values by setting the arm to its various limits and recording the sensor values. Fig 4.11 shows some examples of the limits used for configuration. Once the configuration of all five joints are complete, the user then has the option to save the calibration settings, allowing the same robot arm to be used across different computers without recalibration. Configuration also allow the user see a preview of the robot arm in the preview pane. This allows them to easily move the arm using sliders provided by the main display tab.

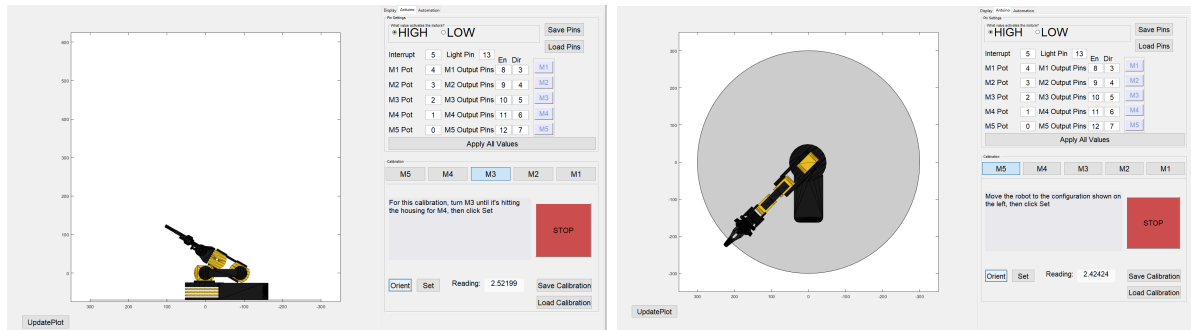


Figure 4.11: Limits used for calibrating the robot’s sensors. By moving the robot to the known extremes of its joints, any value within the limits can be achieved with a simple mapping calculation

4.5.2 Automation

Since the main intent of the GUI was to help students with little to no programming experience, the GUI includes an automation tab. The student simply moves the robot arm to a configuration with the virtual or physical remote—switching between physical and virtual control requires moving a manual switch—and then saves each Configuration. Fig 4.12 shows a saved chain of 11 different configurations. The user then has the option of previewing their created movement path and sending it to the robot arm. Using this system, users can share movement paths between themselves, since the configurations work independently of calibrations. This means that a given pair of robot arms that are accurately calibrated can run the same movement file without issues. This system also allows a user to program movement paths for the robot without having one physically attached. Since the configurations are saved from the configuration of the robot in the preview pane, the display tab sliders can be used to move the preview around, and its configuration can be saved that way.

4.6 Pre-semester Prep

Before the semester begins, the acrylic gears (<https://github.com/BIsichei/OWI-GUI/tree/master/PotHolders/Cut>) are cut, the 3D printed parts (<https://github.com/BIsichei/OWI-GUI/tree/master/3DPrintedParts>) are printed, and the robot arm is assembled.

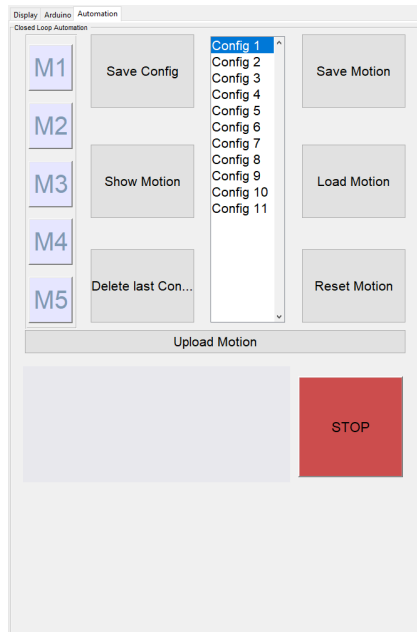


Figure 4.12: The automation tab of the GUI. The buttons on this tab help the user program different movement paths.

com/BIsichei/OWI-GUI/tree/master/PotHolders/Print) are made, and the following parts are ordered:

1. 6 x Spacers <http://a.co/d0hwODm> (50 for \$12)
2. 12 x Bolts <http://a.co/1I0LdLH> (60 for \$6)
3. 1 x Push Button Switch <http://a.co/5Wwy4IX> (100 for \$7)
4. 1 x Custom PCB https://oshpark.com/shared_projects/iEyo6nkB (3 for \$13)
5. 1 x Hex Inverter <https://www.digikey.com/products/en?keywords=296-1566-5-ND>
(10 for \$46)
6. 1 x 14 pin IC Socket <https://www.digikey.com/products/en?keywords=ED3045-5-ND>
(10 for \$18)
7. 1 x (2 x4) Shunt <https://www.digikey.com/products/en?keywords=sam9108-nd>
(all connections need to be soldered together to form a switch) (10 for \$17)

8. 1 x Dual Straight Female Headers (2x6) <https://www.pololu.com/product/1026>
(10 for \$7)
9. 1 x Dual Straight Male Headers (2x40) <https://www.pololu.com/product/966>
(25 for \$30)
10. 1 x Jumper wire kit (40 M/F, 40 M/M, 40 F/F) <http://a.co/hCFAGPP> (\$7)

The quantities indicated are the amounts needed for each student.

The students are expected to purchase:

1. 1 x OWI Robot Arm kit <http://a.co/7EPgoxR> (\$38)
2. 1 x Arduino Mega <http://a.co/acu1G9b> (\$15)
3. 3 x L298 Motor Drivers <http://a.co/3N7bQEp> (5 for \$15)
4. 5 x Rotary Potentiometers <http://a.co/aE2m0tu> (10 for \$11)
5. 1 x Any simple lightweight webcam <http://a.co/hAqZq3J> (\$14)

4.7 Results

At the end of the labs, the students leave the class with experience constructing and programming a robot arm. In the course of doing this, they learn robotics terminology, and have an idea about different means of controlling robots and implementing sensory feedback.

Chapter 5

Conclusion

In this thesis, three different robotic manipulators have been described. The first being a liquid nitrogen cooled magnetic manipulator which currently allows for the control of 3 DOF of a cylindrical permanent magnet. This system was able to successfully increase the power output of EM coils using LN2. The second manipulator, similar to the first, was capable of controlling 2 DOF of a pair of spherical magnets. In it, 2 magnetic spheres representing a swarm of robots were used to successfully implement algorithms for navigation using global inputs and non-slip wall contacts. The last system considered was an augmented 5-DOF robotic arm oriented towards introducing students to the world of robotics and automation. The attachments added feedback to the system, the supporting GUI allowed for automation of the arm's movements, and allowed inexperienced programmers to enjoy the thrill of programming a robot.

For future work, the algorithm for the LN2 cooled system will be tweaked to be more efficient and accurate in its control of the permanent magnet. The 2-D manipulation system could be augmented with conical iron cores to further concentrate the magnetic field in the workspace. The vision system can also be upgraded to allow for faster tracking and automating of the navigation process. Finally, for the augmented robotic arm, the custom PCB for interfacing the robot with the drivers and microcontroller can be revised to increase ease of use. The GUI can also be edited to include tabs for image processing, and inverse kinematic motion planing.

References

- [1] “Stereoaxis[®],” <http://www.stereotaxis.com/>.
- [2] B. J. Nelson, I. K. Kaliakatsos, and J. J. Abbott, “Microrobots for minimally invasive medicine,” *Annual review of biomedical engineering*, vol. 12, pp. 55–85, 2010.
- [3] T. Robinson and G. Stiegmann, “Minimally invasive surgery,” *Endoscopy*, vol. 36, no. 01, pp. 48–51, 2004.
- [4] J. Suri, C. Kathuria, and F. Molinari, *Atherosclerosis Disease Management*. Springer New York, 2010. [Online]. Available: <https://books.google.com/books?id=A7XLOcnPCTkC>
- [5] P. Khatri and S. E. Kasner, “Ischemic strokes after cardiac catheterization: opportune thrombolysis candidates?” *Archives of Neurology*, vol. 63, no. 6, pp. 817–821, 2006.
- [6] M. Hamon, J.-C. Baron, F. Viader, and M. Hamon, “Periprocedural stroke and cardiac catheterization,” *Circulation*, vol. 118, no. 6, pp. 678–683, 2008.
- [7] T. Kensicher, J. Leclerc, D. Biediger, D. J. Shah, I. Seimenis, A. T. Becker, and N. V. Tsekos, “Towards MRI-guided and actuated tetherless milli-robots: Preoperative planning and modeling of control,” in *IEEE/RSJ International Conference on Intelligent Robots and Systems (IROS), 2017*.
- [8] J.-B. Mathieu, G. Beaudoin, and S. Martel, “Method of propulsion of a ferromagnetic core in the cardiovascular system through magnetic gradients generated by an MRI system,” *IEEE Transactions on Biomedical Engineering*, vol. 53, no. 2, pp. 292–299, 2006.

- [9] S. Martel, J.-B. Mathieu, O. Felfoul, A. Chanu, E. Aboussouan, S. Tamaz, P. Pouponneau, L. Yahia, G. Beaudoin, G. Soulez *et al.*, “Automatic navigation of an untethered device in the artery of a living animal using a conventional clinical magnetic resonance imaging system,” *Applied Physics Letters*, vol. 90, no. 11, p. 114105, 2007.
- [10] O. Felfoul, A. T. Becker, G. Fagogenis, and P. E. Dupont, “Simultaneous steering and imaging of magnetic particles using MRI toward delivery of therapeutics,” *Scientific Reports*, vol. 6, p. 33567, 2016.
- [11] J. L. Wilson, M. Jenkinson, and P. Jezzard, “Optimization of static field homogeneity in human brain using diamagnetic passive shims,” *Magnetic resonance in medicine*, vol. 48, no. 5, pp. 906–914, 2002.
- [12] O. Felfoul, E. Aboussouan, A. Chanu, and S. Martel, “Real-time positioning and tracking technique for endovascular untethered microrobots propelled by MRI gradients,” in *ICRA’09. IEEE International Conference on Robotics and Automation 2009*. IEEE, pp. 2693–2698.
- [13] M. P. Kummer, J. J. Abbott, B. E. Kratochvil, R. Borer, A. Sengul, and B. J. Nelson, “Octomag: An electromagnetic system for 5-DOF wireless micromanipulation,” *IEEE Transactions on Robotics*, vol. 26, no. 6, pp. 1006–1017, 2010.
- [14] D. Meeker, “Finite element method magnetics,” <http://www.femm.info>, 2010.
- [15] J. C. Simpson, J. E. Lane, C. D. Immer, and R. C. Youngquist, “Simple analytic expressions for the magnetic field of a circular current loop,” NASA, Tech. Rep., 01 2001.
- [16] K. Vollmers, D. R. Frutiger, B. E. Kratochvil, and B. J. Nelson, “Wireless resonant magnetic microactuator for untethered mobile microrobots,” *Applied Physics Letters*, vol. 92, no. 14, p. 144103, 2008.

- [17] S. Shahrokhi, A. Mahadev, and A. T. Becker, “Algorithms for shaping a particle swarm with a shared input by exploiting non-slip wall contacts,” in *IEEE/RSJ International Conference on Intelligent Robots and Systems (IROS)*, 2017.
- [18] K. E. Peyer, L. Zhang, and B. J. Nelson, “Bio-inspired magnetic swimming micro-robots for biomedical applications,” *Nanoscale*, 2013.
- [19] Y. Shirai, A. J. Osgood, Y. Zhao, K. F. Kelly, and J. M. Tour, “Directional control in thermally driven single-molecule nanocars,” *Nano Letters*, vol. 5, no. 11, pp. 2330–2334, Feb. 2005.
- [20] P.-T. Chiang, J. Mielke, J. Godoy, J. M. Guerrero, L. B. Alemany, C. J. Villagómez, A. Saywell, L. Grill, and J. M. Tour, “Toward a light-driven motorized nanocar: Synthesis and initial imaging of single molecules,” *ACS Nano*, vol. 6, no. 1, pp. 592–597, Feb. 2011.
- [21] A. Becker, G. Habibi, J. Werfel, M. Rubenstein, and J. McLurkin, “Massive uniform manipulation,” in *IEEE International Conference on Intelligent Robots and Systems*, Nov. 2013.
- [22] M. Egerstedt and X. Hu, “Formation constrained multi-agent control,” *IEEE Trans. Robotics Automat.*, vol. 17, pp. 947–951, 2001.
- [23] M. A. Hsieh, V. Kumar, and L. Chaimowicz, “Decentralized controllers for shape generation with robotic swarms,” *Robotica*, vol. 26, no. 5, pp. 691–701, 2008.
- [24] S. Chowdhury, W. Jing, and D. J. Cappelleri, “Controlling multiple microrobots: recent progress and future challenges,” *Journal of Micro-Bio Robotics*, vol. 10, no. 1, pp. 1–11, 2015.
- [25] S. Martel, “Magnetotactic bacteria for the manipulation and transport of micro-and nanometer-sized objects,” *Micro-and Nanomanipulation Tools*, pp. 308–317, 2015.

- [26] X. Yan, Q. Zhou, J. Yu, T. Xu, Y. Deng, T. Tang, Q. Feng, L. Bian, Y. Zhang, A. Ferreira, and L. Zhang, “Magnetite nanostructured porous hollow helical microswimmers for targeted delivery,” *Advanced Functional Materials*, vol. 25, no. 33, pp. 5333–5342, 2015.
- [27] A. L. Bertozzi, T. Kolokolnikov, H. Sun, D. Uminsky, and J. Von Brecht, “Ring patterns and their bifurcations in a nonlocal model of biological swarms,” *Communications in Mathematical Sciences*, vol. 13, no. 4, pp. 955–985, 2015.
- [28] B. R. Donald, C. G. Levey, I. Paprotny, and D. Rus, “Planning and control for microassembly of structures composed of stress-engineered mems microrobots,” *The International Journal of Robotics Research*, vol. 32, no. 2, pp. 218–246, 2013.
- [29] T. Bretl, “Control of many agents using few instructions,” in *Proceedings of Robotics: Science and Systems*, Atlanta, GA, USA, June 2007.
- [30] A. Becker, C. Onyuksel, T. Bretl, and J. McLurkin, “Controlling many differential-drive robots with uniform control inputs,” *Int. J. Robot. Res.*, vol. 33, no. 13, pp. 1626–1644, 2014.
- [31] Z. Nosrati, N. Li, F. Michaud, S. Ranamukhaarachchi, S. Karagiozov, G. Soulez, S. Martel, K. Saatchi, and U. O. Häfeli, “Development of a coflowing device for the size-controlled preparation of magnetic-polymeric microspheres as embolization agents in magnetic resonance navigation technology,” *ACS Biomaterials Science & Engineering*, vol. 4, no. 3, pp. 1092–1102, 2018.
- [32] F. Lamiroux and L. E. Kavraki, “Positioning of symmetric and non-symmetric parts using radial and constant fields: Computation of all equilibrium configurations,” *International Journal of Robotics Research*, vol. 20, no. 8, pp. 635–659, 2001.

- [33] T. H. Vose, P. Umbanhowar, and K. M. Lynch, “Sliding manipulation of rigid bodies on a controlled 6-DOF plate,” *The International Journal of Robotics Research*, vol. 31, no. 7, pp. 819–838, 2012.
- [34] S. Salmanipour and E. Diller, “Eight-degrees-of-freedom remote actuation of small magnetic mechanisms,” in *IEEE International Conference on Robotics and Automation*, 2018.
- [35] A. Denasi and S. Misra, “Independent and leader follower control for two magnetic micro-agents,” *IEEE Robotics and Automation Letters*, vol. 3, no. 1, pp. 218–225, Jan 2018.
- [36] E. Diller, J. Giltinan, G. Z. Lum, Z. Ye, and M. Sitti, “Six-degree-of-freedom magnetic actuation for wireless microrobotics,” *The International Journal of Robotics Research*, vol. 35, no. 1-3, pp. 114–128, 2016.
- [37] L. E. Kavraki, P. Svestka, J.-C. Latombe, and M. H. Overmars, “Probabilistic roadmaps for path planning in high-dimensional configuration spaces,” *IEEE transactions on Robotics and Automation*, vol. 12, no. 4, pp. 566–580, 1996.
- [38] S. M. LaValle, *Planning algorithms*. Cambridge University Press, 2006.
- [39] E. M. Purcell, “Life at low reynolds number,” *American Journal of Physics*, vol. 45, no. 1, pp. 3–11, 1977. [Online]. Available: <http://dx.doi.org/10.1119/1.10903>
- [40] M. Rubenstein, C. Ahler, and R. Nagpal, “Kilobot: A low cost scalable robot system for collective behaviors,” in *IEEE Int. Conf. Rob. Aut.*, May 2012, pp. 3293–3298.

